TGF-β blockade drives a transitional effector phenotype in T cells reversing SIV latency and decreasing SIV reservoirs *in vivo*

Jinhee Kim[1], Deepanwita Bose[2]†, Mariluz Araínga[2]†, Muhammad R. Haque[3], Christine M Fennessey[4], Rachel A Caddell[5], Yanique Thomas[3], Douglas E Ferrell[2], Syed Ali[2], Emanuelle Grody[3,9], Yogesh Goyal[3,9,10], Claudia Cicala[6], James Arthos[6], Brandon F Keele[4], Monica Vaccari[5,7], Ramon Lorenzo-Redondo[1,8], Thomas J Hope[3], Francois Villinger[2] and Elena Martinelli[1]

[1]Department of Medicine, Division of Infectious Diseases, Feinberg School of Medicine, Northwestern University, Chicago, IL, USA
[2]New Iberia Research Center, University of Louisiana at Lafayette, New Iberia, LA, USA
[3]Cell and Developmental Biology, Feinberg School of Medicine, Northwestern University, Chicago, IL, USA
[4]AIDS and Cancer Virus Program, Frederick National Laboratory for Cancer Research, Frederick MD
[5]Division of Immunology, Tulane National Primate Research Center, Covington LA, USA
[6]Laboratory of Immunoregulation, National Institute of Allergy and Infectious Diseases, National Institutes of Health, Bethesda, MD, USA
[7]Department of Microbiology and Immunology, Tulane University School of Medicine, New Orleans, LA, USA
[8]Center for Pathogen Genomics and Microbial Evolution, Northwestern University Havey Institute for Global Health, Chicago, IL, USA.
[9]Center for Synthetic Biology, Northwestern University, Chicago, IL, USA
[10]Robert H. Lurie Comprehensive Cancer Center, Feinberg School of Medicine, Northwestern University, Chicago, IL, USA

† Equal contributors
*Corresponding author:

Elena Martinelli

elena.martinelli@northwestern.edu

One-sentence summary:

TGF-β blockade drives an effector phenotype in immune cells leading to SIV latency reversal and enhanced immune responses in vivo.

Abstract

HIV-1 persistence during ART is due to the establishment of long-lived viral reservoirs in resting immune cells. Using an NHP model of barcoded SIVmac239 intravenous infection and therapeutic dosing of the anti-TGFBR1 inhibitor galunisertib (LY2157299), we confirmed the latency reversal properties of *in vivo* TGF-β blockade, decreased viral reservoirs and stimulated immune responses. Eight SIV-infected macaques on ART were treated with four 2-week cycles of galunisertib. ART was discontinued 3 weeks after the last dose, and macaques euthanized 6 weeks after ART-interruption (ATI). 7 out of 8 macaques rebounded between week 2 and 6 post-ATI. Galunisertib led to viral reactivation as indicated by plasma viral load and immunoPET/CT with ^{64}Cu-DOTA-F(ab')$_2$-p7D3-probe. A decrease in cell-associated (CA-)SIV DNA was detected in lymph nodes, gut and PBMC, while intact pro-virus in PBMC decreased by 3-fold. No systemic increase in inflammatory cytokines was observed. High-dimensions cytometry, bulk, and single-cell (sc)RNAseq revealed a shift toward an effector phenotype in T and NK cells characterized by a progressive downregulation in TCF1.

In summary, we demonstrated that galunisertib, a clinical stage TGF-β inhibitor, reverses SIV latency and decreases SIV reservoirs by driving T cells toward an effector phenotype, enhancing immune responses *in vivo* in absence of toxicity.

Introduction

Interruption of antiretroviral therapy (ART) leads to rapid rebound of viremia in the vast majority of people living with HIV-1 (PLWH) due to the establishment of a persistent HIV-1 reservoir early after infection(*1, 2*). A key mechanism of this persistence is the ability of HIV-1 to enter a state of virological latency characterized by the silencing of viral gene expression and/or lack of viral proteins translation(*3, 4*). This allows the virus to remain invisible to the immune system and latently infected cells to survive and proliferate by homeostatic or antigen-driven proliferation(*5, 6*). Of note, the viral reservoir was initially thought to be stable. However, recent evidence suggests that stochastic HIV reactivation under ART occurs, and selective killing is favored in cells bearing replication competent virus integrated in transcriptionally active sites within the genome(*7-9*). Hence, integration site, but especially the activation status of the infected cells profoundly influences HIV-1 persistence.

Ongoing efforts to achieve a functional cure for HIV-1 are directed towards supplementing ART with immunotherapies targeting the viral reservoir. Such strategies, under the umbrella of “shock and kill”, aim to reactivate the replication competent reservoir and eliminate latently infected cells by viral cytopathic effects or immune-mediated killing (*10, 11*). However, these strategies have thus far failed to achieve a reduction of the viral reservoir or post-ART virologic control in either the clinic or preclinical models. This is mainly due to the low inducibility of latent proviruses and the heterogeneity of the mechanisms of persistence(*12, 13*) (*14, 15*). In contrast, therapeutic vaccination strategies focused on enhancing HIV/SIV-specific responses have had some discreet measure of success(*16*). However, currently, no single strategy leads simultaneously to latency reversal and stimulation of effective immune responses.

The HIV life cycle and HIV’s ability to replicate efficiently are especially dependent on the activation status of the infected cells. In this context, significant advances have been made to directly activate immune cells through non-canonical pathways in order to promote HIV latency reversal(*17*). However, the activation and differentiation of immune cells is intrinsically linked to

80 cellular metabolism(*18*). Indeed, signaling pathways that govern immune cell differentiation and
81 activation such as mTOR and Wnt/β-catenin, not only have been implicated in regulating HIV
82 latency(*19-21*), but are also critical regulators of cell metabolism(*22*). The metabolic status of an
83 infected cell, in turn, plays a critical role in its ability to support latency reactivation and viral
84 production(*19, 23*).
85 In this context, recent evidence suggests that TGF-β plays a critical role in the regulation of
86 immune cell activation and metabolic reprogramming(*24-26*). Specifically, in the context of $CD8^+$
87 T cells, TGF-β has been shown to suppress mTOR signaling preserving the metabolic fitness of
88 memory $CD8^+$ T cells(*25*) and stem-like antigen specific $CD8^+$ T cells through its modulation of
89 Wnt/β-catenin factor TCF1(*26, 27*). TCF1 and the mTOR pathway are also critical to T cell
90 differentiation and responsible for the transition from activated effector cells to resting memory
91 cells during LCMV infection(*22, 26*). The regulation of quiescence in $CD8^+$ T cells that follows
92 continuous TGF-β stimulation is critical to the transition to a memory phenotype and it is driven
93 by specific metabolic changes that are linked to decreased glycolytic activity, more efficient
94 mitochondrial respiration, and long-term survival(*25, 26*).
95 Similarly, in the context of NK cells, TGF-β has been implicated in decreasing their baseline
96 metabolism driving lower expression of markers of NK cytotoxic activity(*28*).
97 While TGF-β-mediated suppression of TCR and IL-2 signaling were shown to lead to lower $CD4^+$
98 T cell activation following cognate antigen recognition in older studies(*24, 29*), more recent work
99 using $CD4^+$ T cell-specific deletion of the TGF-β receptor demonstrated an even more profound
100 effect of TGF-β on all stages of $CD4^+$ T cell activation, proliferation and cytotoxic response to
101 LCMV than in $CD8^+$ T cells(*30*). However, little is known on the specific role of TGF-β in regulating
102 the transition to and from memory and effector phenotypes in $CD4^+$ T cells and how this may be
103 associated with TGF-β-driven changes in $CD4^+$ T cell metabolism. Moreover, TGF-β regulates the
104 expression of CD103 and other surface and intracellular factors essential of T cell residency in

105 mucosal tissues(*31-33*). Hence, TGF-β is considered the master regulator of mucosal
106 immunity(*34*).
107 We and others have recently demonstrated that TGF-β regulates HIV-1 latency in primary $CD4^+$
108 T cells ex vivo and in vivo(*35-37*). Latency reversal was detected in a non-human primate (NHP)
109 model of HIV infection following a short treatment with a clinical stage TGF-β inhibitor, galunisertib
110 (LY2157299)(*38*). In that study, we documented latency reversal particularly at the level of the gut
111 mucosal tissue using the ^{64}Cu-anti-gp120 Fab_2(7D3) probe and immuno-PET/CT(*35*). We further
112 validated the ability of immune-PET/CT to identify sites of viral reactivation and replication in the
113 gut by performing tissue resection in hot areas of the gut identified by PET followed by
114 confirmatory PCR for vDNA/RNA and vRNAscope(*35*).
115 Herein, we demonstrate how treatment with galunisertib with a 2-week on, 2-week off regiment
116 that mimics the therapeutic regimen employed in the clinic in phase 1 and 2 trials of solid
117 tumors(*39, 40*), leads to profound transcriptional and functional changes in immune cells in the
118 absence of overt toxicity or increased systemic inflammation. Importantly, we observed a shift
119 toward a transitional effector phenotype in $CD4^+$ T cells and other immune cells both systemically
120 and in the lymph nodes. This shift was accompanied by, and likely responsible for, increased viral
121 reactivation in SIV-infected, ART treated macaques documented by molecular techniques and
122 PET/CT images. At the end of the treatment with galunisertib, we detected lower viral reservoir
123 levels, including total and intact proviral DNA in both PBMC, gut and lymph nodes and significantly
124 higher immune responses.
125

126 **RESULTS**

127 **2-weeks on-off therapeutic regiment with galunisertib leads to viral reactivation SIV**
128 **infected, ART-treated macaques.**

129 To confirm galunisertib-driven HIV/SIV latency reversal and investigate the underlying
130 mechanisms, 8 Indian origin rhesus macaques (*Macaca Mulatta*, Mamu-A01-, -B08, -B17-, all

131 females) were infected intravenously with 300 TCID50 of the barcoded SIVmac239M2. We
132 initiated ART treatment (daily co-formulated Tenofovir [PMPA], Emtricitabine [FTC] and
133 Dolutegravir [DTG]) on week 6 post-infection (pi). A 2-week on, 2-week off therapeutic cycle with
134 galunisertib (20mg/Kg twice/daily orally) started at week ~35pi and continued for a total of 4 cycles
135 (Fig 1A and Table S1). ART was discontinued 3 weeks after the last galunisertib dose, and the
136 macaques were followed for 6 weeks after ART discontinuation. Median peak plasma viral load
137 (pVL) was 10^8 copies/mL at week 2pi. Given the synergistic activity of anti-PD1 and anti-TGF-β
138 therapies in cancer(*41, 42*), a rhesus anti-PD1 antibody was administered at 5mg/kg before the
139 3rd and 4th cycle to 2 macaques (08M156 and A6X003). However, no differences were noted for
140 these 2 macaques in any of the parameters we measured, and the data were pooled.
141 Full suppression to undetectable levels (pVL LOD 15 copies/mL) was achieved in 3 out of the 8
142 macaques at week 10pi. In the other 5 macaques, pVL fell below 65 copies/mL by week 22pi with
143 a single blip of 400 copies/mL in A8T010 at week 29pi (Fig 1B). Following the start of the
144 galunisertib treatment, pVLs increased in 7 out of 8 macaques from a single peak over
145 undetectable in 08M171 and A8L057 to several peaks and up to 10^3 copies/mL in the other
146 macaques. Of note pVLs in A8T010 and A8R095 was undetectable for over 5 weeks before,
147 respectively, blips of up to 10^2 copies/mL were detected following galunisertib treatment initiation
148 (Fig 1B). More frequent blips were noted during the first 2 cycles with galunisertib compared to
149 cycles 3 and 4 (Fig 1C). However, 08M171 and A8L057 did not experience a pVL increase until
150 the 4th cycle.
151 Importantly, in support of the pVL data above, we documented viral reactivation also using
152 immunoPET/CT. The ^{64}Cu-anti-gp120 Fab_2(7D3) probe was injected 24hrs before each scan and
153 scans performed before the first and after the last galunisertib dose in each cycle. As shown in
154 Fig 2, Fig S1 and Movies S1-S8, the PET signal visibly increased in different tissue areas after
155 cycle 2 (in A8R095, 08M156, A8L014 and A8T010) or at the beginning of cycle 3 (in A6X003,
156 08M134 and A8L057). In 08M171 we observed an increase in the gut area only at the beginning

157 of cycle 2. An unforeseen issue with probe stability in cycle 3 led to exclusion of the last 2 scans
158 of 08M171 from the analysis (Fig S1, 08M171 infection, treatment and scan were offset compared
159 to the other macaques). A corresponding increase in mean standard uptake values (SUV) was
160 detected in the gastrointestinal area and axillary lymph nodes (Fig 2B) and was significant in cycle
161 3 compared to before cycle 1 (BC1). In these anatomical areas (ROIs in Fig S2 and Movies 9-
162 10), SUV increases likely correspond to increases in viral replication as demonstrated in previous
163 studies(*43, 44*). A PET signal increase was also noted in the area of the vertebral column (spine)
164 and nasal associated lymphoid tissues (NALT). However, neither cerebrospinal fluid (CSF) nor
165 bone marrow (BM) or NALT tissue were collected during the study, and we have no prior validation
166 of the specificity of the signal in these anatomical locations. Hence, whether this signal
167 corresponds to increased viral replication and whether this occurs in the vertebral bones or
168 cerebrospinal fluids remains to be determined. No SUV increase was present at the level of the
169 spleen or kidney, where probe accumulation and background signal likely masked any specific
170 signal. However, a significant increase in SUV was detected in the liver (Fig 2B). Similar increases
171 in PET signal are also evident when considering the SUV Total in these anatomical areas (Fig
172 S3A). Moreover, blood pool activity (BPA) also increased during the 3rd cycle (Fig S3B). Whether
173 this was due to galunisertib-specific effects on probe pharmacokinetics, changes in viral antigen
174 or probe-antigen kinetics remains to be determined. However, when the mean SUV was
175 normalized for BPA in the gut, axillary lymph nodes and spine, the signal increase in the 3rd cycle
176 was lost, but an increase during the first cycle became evident (Fig S3C). Of note, the non-BPA
177 normalized SUVmean increase in the gut and lymph node areas in most cases followed an
178 increase in cell-associated vRNA detected, respectively, in colorectal biopsies and fine needle
179 aspirates (FNA) at the same time points during treatment (Fig S4).
180
181 **Decreased viral reservoir in absence of systemic inflammation after 4 cycles with**
182 **galunisertib**

183 To determine the impact of galunsiertib on SIV reservoir, we measured CA-vDNA in PBMC,
184 colorectal biopsies and lymph nodes (LN). A significant decrease in CA-vDNA was detected in all
185 tissues between week 35pi (beginning of cycle 1, BC1) and week 49pi (after/end of cycle 4, AC4)
186 for gut and LN, and between week 35pi (BC1) and end of cycle 3 (AC3) for PBMC (Fig 3A, AC4
187 not measured for PBMC and Fig S5A). In the gut and LN (right axillary), decreases ranged from
188 a Log to 1/3 of a Log (gut: median 0.77; range: 0.33 - 0.94 fold LN: median: 0.93; range: 0.33-
189 0.98 fold decrease). In the PBMC the decrease was slightly less pronounced with a median half
190 Log decrease (median: 0.58; range 0.28 - 0.88 fold decrease). However, the comparison for the
191 PBMCs was between week ~35 and week ~45 (end of cycle 3, AC3) instead of the end of all 4
192 cycles, because a snap frozen pellet was not available at the end of cycle 4 for PBMCs. The SIV
193 reservoir in PBMCs was also monitored by SIV-IPDA (intact proviral DNA assay) comparing
194 before cycle 1 (BC1) to the end of cycle 4 (AC4). Of note, we observed significant decreases of
195 both total and intact provirus by SIV-IPDA. Intact provirus declined similarly to the CA-vDNA with
196 a median of half Log (median: 0.53; range: 0-0.71 fold decrease).
197 In contrast, no decline in CA-vDNA was detected in the PBMCs of a group of 4 macaques infected
198 intravenously with the same stock of SIVmac239M2 for a separate study. These 4 macaques
199 were placed on ART on week 6pi as in our study. However, they were infected several months
200 after our study and samples collected at similar time points varied in their availability. No decline
201 in CA-vDNA was detected under ART, between weeks 28 and 52pi (untreated group, Fig S5B).
202 This suggests that the decline in CA-DNA in our study was not due to ART alone. However, in
203 absence of an appropriate control group, it is not possible to be determine with confidence the
204 relative contribution of ART and galunisertib to the decline.
205 Importantly, we found no significant changes in any of the clinical variables (chemistry and
206 hematology, Tables S2 and S3) measured before, during and after the galunisertib therapy.
207 Moreover, we observed no changes in the concentrations of inflammatory chemokines and
208 cytokines measured in plasma before and after the first 2 treatment cycles and at the end of the

209 last cycle (Fig 3C). The only difference in cytokine and chemokine levels after galunisertib
210 treatment was a small increase in IL-10 detected at the end of the last cycle compared to before
211 treatment (Fig S5C).
212
213 **Galunisertib treatment drives an effector phenotype in T and NK cells.**
214 The phenotype of PBMCs before and after Galunisertib treatment was monitored by high-
215 parameter flow cytometry of T and NK cell subsets and phenotype (Table S4). Classical subsets
216 and single-color analysis of MFI revealed a substantial increase in the expression of CD95 and a
217 profound consistent decrease in TCF1 expression in $CD4^+$ T cells that continued throughout the
218 treatment (Fig 4A). In contrast, a small decrease in CD62L after the first cycle, reverted to baseline
219 during the following cycles. The frequency of naïve cells, defined as $CD95^-$ within $CD4^+$ T cells,
220 decreased in parallel with the increase in CD95 (gating strategy in Fig S6). Interestingly, there
221 was no change in the expression of CCR7 or CD28 within $CD95^+$ $CD4^+$ T cells (Fig 4B). Hence,
222 the frequency of central memory and effector memory as defined by CD95 and CD28 or CCR7
223 did not change (Table S5). The levels of T-bet did not change significantly (Fig S7A). However,
224 we detected a downregulation of the gut homing receptor integrin $\alpha4\beta7$ and a decrease in the
225 levels of granzyme B (GRZB, Fig S7A). Of note, the expression of activation markers CD69, HLA-
226 DR and Ki67 remained mostly unchanged, with the exception of an increase in HLA-DR at the
227 beginning of cycle 2 compared to before galunisertib (Fig 4C). Interestingly, the effect of
228 Galunisertib on $CD8^+$ T cells was not as pronounced as it was on $CD4^+$ T cells. No significant
229 increase was detected in CD95 expression and TCF1 downregulation reached significance only
230 at the end of the treatment (Fig 4D). Markers of cell activation like HLA-DR, Ki67 and CD69 did
231 not change (Fig 4D and Fig S7B). However, we detected a significant decrease in T-Bet at the
232 beginning of cycle 2 (BC2) compared to before treatment (BC1). Finally, in contrast to $CD4^+$ T
233 cells, the decrease in GRZB was more pronounced at several time points during treatment and
234 there was a sustained significant increase in CCR7 expression in memory $CD8^+$ T cells (Fig 4E).

235 Interestingly, the expression of PD1 on both $CD4^+$ T cells and $CD8^+$ T cells either did not change
236 or was slightly downregulated. Importantly, the frequency of $PD1^+$ $CD101^+$ ($TCF1^{low}$) exhausted
237 memory $CD8^+$ T cells(*45*) did not change (Fig S7B). Finally, within $NKG2A^+$ $CD8^+$ NK cells, there
238 was a pronounced increase in CD16 expression and an initial increase in the proliferation marker
239 Ki67 (AC1 vs BC1; Fig 4F).
240 High-dimensional data visualization with tSNE and clustering analysis with FlowSOM(*46*)
241 confirmed the results of the classical analysis. We performed tSNE and FlowSOM after data clean
242 up with FlowClean and normalization with the SwiftReg algorithm(*47*). We performed two
243 analyses. One analysis compared before (BC1) and after the last cycle (AC4) only (Fig 4G and
244 Fig S8A). A second analysis was performed on all time points (Fig S8B and S8C). When we
245 compared only BC1 and AC4, the PhenoGraph clustering algorithm identified 36 populations.
246 FlowSOM with 36 populations identified 6 populations of $CD4^+$ T cells, 6 of $CD8^+$ T cells and 4 of
247 NK cells ($NKG2A^{high}$ $CD8^+$; Fig S8A). The remaining populations were likely monocytes and other
248 minor subsets. Direct comparison of each population revealed a decrease in Pop 31 (naïve CD8
249 T cells) and Pop 30 (central memory $Ki67^+$ $CD8^+$ T cells) and an increase in Pop 2 and 3 (effector
250 and central memory $CD4^+$ T cells). Finally, there was a decrease in HLA-DR high Pop0 and an
251 increase in $CD16^{high}$ $NKG2A^-$ Pop14 (Fig 4H and S8A). Visual inspection of the tSNE plots (Fig
252 4G) revealed 3 areas mostly occupied by cells in the post-galunisertib AC4 group (New1, 2 and
253 3) which were characterized by high levels of CD16 and GRZB (New 3 is likely NK cells). In
254 contrast, 3 areas mostly occupied by cells in the pre-galunisertib group BC1 (Old1, 2 and 3) were
255 characterized by high levels of TCF1 and low CD95, confirming the finding of the classical
256 analysis. Analysis of all time points with phenograph-derived 38 populations in FlowSOM
257 recapitulated findings obtained with the classical analysis and the BC1 AC4 comparison with no
258 additional insights (Fig 4I).
259
260 **Galunisertib treatment in vivo increases pTreg while decreasing pTfh**

261 The frequencies of circulating Tregs and Tfh cells were monitored with an established flow
262 cytometry panel(*48, 49*) after the first and third cycle of galunisertib. The frequency of all $CD4^+$
263 Tregs ($CD25^{high}$ $FoxP3^+$; gating in Fig S9) and $CD8^+$ Tregs increased after the first cycle and
264 remained higher until the end of the 3rd cycle, while $CCR4^+$ Treg were proportionally higher at the
265 end of the treatment compared to before (Fig 4J). In contrast, circulating Tfh ($CXCR5^+$ $PD1^+$;
266 gating in Fig S9) were lower at the end of the Galunisertib treatment both within total and central
267 memory $CD4^+$ T cells (Fig 4J). Finally, the expression of CD39 (ecto-nucleotide triphosphate
268 diphosphohydrolase 1), which tracks within extracellular adenosine and immunosuppressive
269 effects, was lower on total and central memory $CD4^+$ T cells (Table S5 and Fig 4J, respectively).

270

271 **Bulk RNAseq of PBMC and single-cell (sc)RNAseq analysis of LN confirm a profound shift**
272 **toward effector phenotype.**

273 In our previous studies, we determined that 6hrs after galunisertib treatment in naïve macaques
274 there was an upregulation of the AP1 complex (JUN and FOS) and several genes encoding
275 ribosomal proteins in $CD4^+$ T cells(*44*). To understand early and later effect of galunisertib in the
276 context of SIV infection, in the current study we performed bulk RNAseq of PBMC isolated 1hr
277 after the first administration of galunisertib in cycle 1 and at the end of the 1st 2-weeks cycle. We
278 found 640 genes significantly modulated (FDR<0.05; abs(log_2 FC(Fold Change))>2) in PBMC just
279 1hr after the first dose of galunisertib. The majority (457 genes) were downregulated (Fig 5A).
280 Gene set enrichment analysis (GSEA) revealed an upregulation of the oxidative phosphorylation
281 (OXPHOS; Enrichment Scores (ES) 0.58 FDR=0.048) and the reactive oxygen (ES 0.55
282 FDR=0.075) pathways among the Hallmark genet sets (Fig 5A and S10). Among the Biocarta
283 sets, there was an enrichment in the electron transport chain (ETC; ES 0.84 FDR=0.132) and a
284 downregulation of the circadian (ES -0.81 FDR=0.163) pathways (Fig 5A and S10). Finally, among
285 the top modulated genes (by FC), we identified several genes encoding for soluble transporters,

286 while classical activation markers like CD69 and CD38 were downregulated (Fig S10B). An early
287 engagement of metabolic pathways was confirmed by enrichment analysis of significant DEG with
288 Metascape(*50*) with an upregulation of adipogenesis, OXPHOS and fatty acid metabolism (Fig
289 S10C). Of note, 2 weeks after the beginning of galunisertib, metabolic pathways were still among
290 the most enriched upregulated pathways in PBMCs (Fig 5B and Fig S11A). Among the top
291 upregulated genes there were CD44, CCR5, several integrins and GRZA and GRZB (Fig S11B).
292 Finally, we performed bulk RNAseq of rectal biopsy tissue before and after the first cycle with
293 galunisertib (Fig 5C). There were only 51 differentially expressed genes (DEGs; FDR<0.05;
294 $\log_2$FC=2). GSEA analysis of all DEGs (FDR<0.05) revealed the G2_M_DNA replication pathway
295 highly enriched (ES 0.97 FDR=0.012) within the Hallmark set. Among the most interesting
296 changes, we observed a pronounced downregulation of integrin β7, in contrast to an increase in
297 integrin αE (CD103; Fig 6C), suggesting that TGF-β-driven increase in αE(*51*) may be driven by
298 non-canonical TGF-β pathway signaling not blocked by galunisertib.
299 To clarify the impact of galunisertib at the single cell level and in lymphoid tissues, we also
300 performed scRNAseq analysis of cells isolated from LNs before (right axillar) and after (right or
301 left inguinal) the first cycle (Fig 6). Dimensionality reduction and clustering analysis with PCA and
302 uniform manifold approximation and projection (UMAP)(*52*) was performed to visualize the data
303 (Fig 6A). However, cells were classified based only on gene expression (Fig 6B and C). We first
304 classified major subsets: T cells (38,705 cells), B cells (31,385 cells), NK cells (1,628 cells),
305 macrophages (285) and cells expressing both CD19 and CD3 (942 T/B cells) (Fig 6A shows this
306 classification over UMAP). Then we classified only $CD4^+$ and $CD8^+$ T cell subsets (Fig 6C and
307 S12A) and B/T subsets including naïve and germinal center (GC) B cells and Tfh cells (Fig S12B
308 and S12C). Cell number for all these subsets did not change with treatment (Fig S13). However,
309 differential gene expression analysis of T cells revealed an upregulation of members of the AP1
310 complex, CD69, β2 macroglobulin and RPL13 among the most upregulated genes (Fig 6D).

311 Moreover, it confirmed a downregulation of TCF1 at the transcriptional level (TCF7 gene; Fig 6D).
312 Gene enrichment analysis revealed again Myc_targets_V1, OXPHOS and mTORC1 as the most
313 enriched hallmark pathways (Fig 6E). Of note, among gene ontology cellular processes, RNA
314 processing was the most highly enriched pathway, followed by intracellular transport and catabolic
315 processes following right after (Fig S14A) confirming an increase in translation and metabolism
316 within these cells.
317 Since we noticed substantial differences in the impact of galunisertib on $CD4^+$ T cells compared
318 to $CD8^+$ T cells by flow, we focused the analysis on these subsets. In $CD4^+$ T cells we found only
319 25 DEGs with a $log_2FC=0.15$, while 34 DEGs were in $CD8^+$ T cells with more downregulated
320 genes in the $CD8^+$ T cells compared to the $CD4^+$ T cells. The AP1 complex and TCF7 were again
321 upregulated and downregulated respectively in both $CD4^+$ (Fig 6F) and $CD8^+$ T cells (Fig 6G).
322 However, STAT1 was more strongly downregulated in $CD4^+$ T cells. Enrichment analysis showed
323 once again upregulation of Myc_targets_V1, OXPHOS and mTORC1 pathways in both $CD4^+$ and
324 $CD8^+$ T cells (Fig 6H and Fig S14B). Interestingly, the most enriched set among in Biocarta was
325 the HIV-Nef pathway (Fig 6I) demonstrating the relevance of these galunisertib-driven changes
326 to HIV cell cycle and transcription (highly enriched KREB pathway as well). The 2nd most enriched
327 Biocarta pathway was TCR signaling, linking galunisertib to cell activation. Next, we analyzed
328 changes in gene expression in Tfh cells. In this subset we obtained a similar number of DEG as
329 in other T cells and myc_targets_V1 was still the most enriched hallmark pathway (Fig S14C and
330 D). In B cells, the AP1 complex was again prominently upregulated, together with CD83, CD69
331 and MAMU-DR. Of note, more genes were modulated in B cells (44 genes with a $log_2FC=0.15$
332 and 18 with logFC0.2) than in T cells with some differences in enriched pathways (Fig S14F).
333 Similar genes were modulated in GC B cells and naïve B cells with several more DEGs in naïve
334 B cells than in GC cells (Fig S15A and B). Finally, 144 genes were modulated in NK cells and 39
335 genes in macrophages (Fig S15C and D; $log_2FC=0.15$). GRZB was prominently upregulated, but
336 CD44 downregulated. In macrophages genes were mostly downregulated including TCF7L2 and

337 KLF4 suggesting an increase in inflammatory phenotype and decrease in M2 polarization(*53*) (Fig
338 S15D).
339
340 **Galunisertib increases SIV-specific responses and changes barcode distribution**
341 In order to understand how galunisertib affected immune cell function and SIV-specific responses,
342 we stimulated PBMC with 15-mer SIV peptides from SIVmac239 gag, pol and env for 24hrs on
343 antibody coated Elispot plates. Because of sample availability, we probed before and after the
344 first cycle and after the 3rd galunisertib cycle only. Interestingly, by the end of the 3rd cycle there
345 was a significant increase in IFN-γ secretion both SIV-specific (particularly against env) and non-
346 specific (DMSO control). A notable increase in TNF-α release was similar in response to Gag and
347 non-specifically (Fig 7). In contrast, IL-2 release appeared to increase slightly after the first cycle
348 (non-significant), but remained unchanged with a slight decrease by the end of the 3rd cycle (Fig
349 7).
350 In order to understand if these changes in immune responses in combination with latency reversal
351 and switch toward an effector phenotype may have impacted viral population dynamics, we
352 analyzed changes in numbers and distribution of the viral barcodes before and after the first 3
353 treatment cycles. There was no barcode amplification at several time points particularly in the
354 lymph nodes. However, although there were no significant changes in the number or diversity
355 (measured as Shannon Entropy; Sh) of barcodes before and after each galunisertib cycle (Fig
356 S16A and Fig 8A), we found significant changes in barcode frequency distribution in most tissues
357 and cycles after galunisertib treatment (Fig 8B and S16B). Specifically, the relative proportion of
358 each barcode changed in all monkeys in all cycles in the rectal biopsies (probably a consequence
359 of different sampling area), but also for all LN analyzed (except for 08M134 in cycle 1). Of note,
360 the same LN were sampled at the beginning and after cycle 3 (Table S6). Hence, sampling
361 location does not explain the changes barcode distribution. Changes in the proportion of barcodes

362 were also detected in at least half of the PBMCs after cycle 1 and 2 (cycle 3 not analyzed). Finally,
363 barcode diversity decreased in plasma post-ATI compared to the time point right before ART (Fig
364 8C) and barcode distribution significantly changed post-ATI compared to pre-ART in 2 of the 7
365 macaques that rebounded (Fig S16C).
366
367 **TCF1 downregulation in CD4$^+$ T cells correlates with virological and immunological**
368 **endpoints.**
369 In order to explore a possible association between the various virological and immunological
370 parameters and their changes, we built a correlation matrix with a curated set of variables of
371 interest or their fold changes. This analysis revealed an association between the decrease in
372 TCF1 expression in the CD4$^+$ T cells and several virological and immunological variables (Fig
373 8E). Specifically, both the levels of CA-vDNA in the colorectal tissue and the fold increase in gut-
374 SUV strongly inversely correlated with fold changes in TCF1. Since TCF1 decreased, a larger
375 decrease in TCF1 was directly proportional to residual vDNA in the gut at the end of cycle 4 and
376 to the increase in PET signal in the gut (Fig 8D and 8E). A weaker, but still significant association
377 was also present with CA-vDNA in PBMC at the end of cycle 3 and with the levels of vRNA in the
378 lymph nodes at the end of the 4th cycle (Fig 8D and S17A). Finally, the decrease in TCF1
379 correlated with the increase in IFN-γ and poly-functional IFN-γ/TNF-α releasing cells (cumulative
380 increase of SIV-specific responses to gag, pol and env; Fig 8D and 8E). Of note, the increase in
381 PET signal in the gut also correlated with the levels of vDNA in PBMC at the end of cycle 3, vDNA
382 in gut biopsies and residual CA-vRNA in LN at the end of cycle 4 (Fig S17B). Interestingly, the
383 levels of residual CA-vRNA in LN also correlated with the increase in IFN-γ and poly-functional
384 IFN-γ/TNF-α releasing cells (Pearson r=0.85 and 0.76, respectively). Finally, the residual intact
385 pro-virus (IPDA) directly correlated with the levels of IFN-γ and IFN-γ/TNF-α produced in response
386 to SIV peptides at the end of cycle 3 (Fig 8D; r= 0.76 and 0.88, respectively). In contrast, the

387 change in intact provirus trented to correlate inversely with the levels of IFN-γ, so that a larger
388 decrease directly correlated with more IFN–γ responses. However, this did not reach significance
389 (p=0.117, Fig S17C).
390
391 **Discussion**
392 HIV-1 latency in T cells is maintained through diverse mechanisms that include blocks in
393 transcriptional elongation, completion, and splicing(*13*). A common characteristic shared by HIV-
394 1 latently infected cells of both T and myeloid cell lineages is their "resting" phenotype(*14, 54-56*)
395 In these cells, an inability to transcribe proviral DNA is linked to a generalized decrease in
396 transcriptional activity which, in turn, is linked to their metabolic status(*23*). Cellular metabolism is
397 in turn influenced by tissue location and environmental cues(*57*).
398 TGF-β is released at high level in PLWH and its levels remain high during ART(*58-60*). The
399 immunosuppressive activity of TGF-β is well-known. However, the effect of TGF-β signaling in
400 immune cells is highly context dependent(*61*). Hence, TGF-β plays different roles according to a
401 cell differentiation and activation status(*61*). In $CD8^+$ T cells and NK cells, TGF-β was shown to
402 decrease mTOR activity and preserve cellular metabolism (high mitochondrial activity and spare
403 respiratory capacity, but reduced mTOR activity) preventing metabolic exhaustion(*25, 26, 62, 63*).
404 This effect was linked to survival of antigen-specific $CD8^+$ T cells, preservation of their stemness
405 and it was linked to higher expression of the TCF1 factor(*25*).
406 In contrast, in $CD4^+$ T cells TGF-β is known to decrease TCR activation(*29, 64*), restrict
407 proliferation and inhibit cytotoxicity (including granzyme and perforin release) at different stage of
408 infection in vivo(*30, 65*). However, the role of TGF-β in the formation and preservation of $CD4^+$ T
409 cell memory is still unclear(*61*). Moreover, the link between TGF-β signaling and TCF1 expression
410 in $CD4^+$ T cells is unexplored.

411 Here, we used a clinical stage small drug, galunisertib, developed by Eli Lilly and used in several
412 phase 1 and 1/2 clinical studies against solid cancer(*39, 66, 67*) to investigate the impact of TGF-
413 β blockade on SIV latency, SIV reservoir and immune responses. Of note, Eli Lilly did not
414 terminate galunisertib development program because of toxicity(*68, 69*). Indeed, in our studies in
415 macaques, we observed no adverse events nor changes in chemical or hematological variables.
416 Moreover, there were no detectable changes in the levels of the 24 inflammatory factors that we
417 probed in plasma during the treatment. This suggests that this therapeutic approach may be safe
418 in people living with HIV (PLWH).
419 The first important finding of our study was the confirmation of our previous report of the latency
420 reversal properties of TGF-β blockade in vivo(*35*). Indeed, we found increase in pVL in 7 out of
421 the 8 macaques upon initiation of galunisertib therapy. Although not all macaques were fully
422 suppressed before treatment, substantial increases in pVL (>10^2 copies/mL) were noted also in
423 fully suppressed macaques (08M171, A8R095 and A8L057). Moreover, viral reactivation was
424 documented in tissues by immunoPET/CT. Importantly, the SUV increase detected post-
425 galunisertib in gut and LN correlated with CA-vRNA as in our previous studies(*35*) and,
426 interestingly, it was associated with a decrease in TCF1. However, despite this evidence, the
427 absence of imaging studies carried out in uninfected, galunisertib-treated macaques require that
428 we interpret this data with care. This is due mostly to unexpected and, yet unexplained,
429 galunisertib-driven changes in BPA. Without a better understanding of these changes, it is difficult
430 to determine the BPA contribution to the PET signal increase in tissues. Yet, an increase in gut
431 and LN SUV is present even after BPA normalization (although in cycle 1 instead than cycle 3).
432 Since our probe is a $F(ab')_2$ and not a whole antibody, we did not expect the probe to be still
433 present in significant amounts in circulation in a scan performed 24hrs post-probe injection.
434 Nonetheless, galunisertib may have impacted probe and probe-antigen complex
435 pharmacokinetics or the probe interaction with increased viral antigen. TGF-β is required for
436 vascular barrier function(*70*). Hence, galunisertib may have increased vascular permeability.

437 However, this would have driven a major decrease in BPA instead than the detected increase.
438 Moreover, significant changes in VEGF-A, a factor critical to and tracking with vascular
439 permeability(*71*), were not noted. This, in conjunction with our previous studies which validated
440 the specificity of the PET signal for areas of enhanced SIV replication in gut and lymph nodes(*35,*
441 *43, 72*), demonstrates that the galunisertib-driven increases in SUV were likely specific, and
442 identified areas of SIV latency reversal at least in gut and lymphoid tissues. The extent to which
443 the increased signal in the spine and bones recapitulates an increase in SIV replication at these
444 sites remains to be determined.
445 Importantly, we observed a decrease in CA-vDNA in all the tissues that cannot be attributed to
446 ART alone. Indeed, although we did not have a concurrent control group, this decrease was not
447 present in similar studies conducted in SIVmac239M2 infected macaques on the same ART
448 regimen, but not treated with galunisertib. Considering studies by other groups with different
449 models (SIVmac251), they report 2nd phase decay of SIV intact provirus (weeks ~32 to ~100pi,
450 Fig 2B in(*73*)) with a $t_{1/2}$ of >8 months(*73*). In contrast, in our study, the intact provirus decreased
451 by 3 fold (median) in a little over 3 months (from week 35pi, BC1 to week 49pi, AC4). Interestingly,
452 this decrease in intact pro-virus trended toward a direct correlation with IFN-γ responses.
453 However, IFN–γ levels also inversely correlated with the absolute value of residual intact provirus,
454 suggesting that IFN-γ responses were driven by residual viral reservoir while, at the same time,
455 were involved in clearing intact virus. Indeed, the increase in IFN-γ and TNF-α also correlated
456 with residual CA-vRNA in the LN at the end of the treatment. The latter, in turn, was directly
457 proportional to the increase in gut SUV. This is in line with increased latency reversal explaining
458 residual viral RNA in lymphoid tissues.
459 Finally, one of our most intriguing results was the profound downregulation of TCF1 in $CD4^+$ T
460 cells at both the transcriptional and protein levels. Although TCF1 is conventionally viewed as an
461 effector of the canonical Wnt pathway(*74*) and recently reached notoriety for its role in maintaining

462 stemness of antigen-specific memory CD8$^+$ T cells(*26, 75*), TCF1 has a plethora of functions in T
463 cell development and differentiation largely independent of Wnt signaling(*22*). In CD4$^+$ T cells,
464 TCF1 has been implicated in orchestrating all the major Th subsets, including Th1, Th2, Th17
465 and Tfh(*76*). TCF1 is known to control the bifurcation between Th1 and Tfh in favor of Tfh
466 cells(*76*), while it negatively regulates Treg development(*22*). This is in line with our findings of
467 increased Treg and decreased Tfh, in the midst of a profound downregulation of TCF1.
468 Importantly, TCF1 is downregulated with increased cellular differentiation and progression toward
469 effector functions in T cells. T cell activation leads to reduced levels of TCF1 and higher levels of
470 TCF1 are present in T cells with higher stemness and low anabolic metabolism(*74*). These
471 findings suggest that TCF1 has a critical role in maintaining quiescence in immune cells likely in
472 concert with TGF-β(*18, 65*). Our data reveal that this link may be even more prominent and
473 important in CD4$^+$ T cells than in CD8$^+$ T cells. Importantly, the decrease in TCF1 was
474 accompanied with enhancement in other effector markers such as CD95, CD16 and GRZB (at
475 the transcriptional level) and an increase in the transcription of AP1 complex. However, there was
476 no clear upregulation of other classical markers of immune activation such as CD69 and no
477 increase in T cell proliferation (Ki67 expression). Hence, galunisertib treatment does not appear
478 to lead to classical T cell activation nor to an increase in a specific terminally differentiated effector
479 subset. Instead, in vivo TGF-β blockade seems to primarily change the metabolic state of T cells
480 (and likely other immune cells) increasing OXPHOS and mitochondrial function. Of note, although
481 glycolysis is essential during cell activation, mitochondrial pathways are engaged and remodeled
482 early after activation and OXPHOS upregulation has a pivotal role in the earliest stages of cell
483 activation(*18*).
484 Hence, we propose a model in which TGF-β inhibition forces cells (particularly CD4$^+$ T cells) out
485 of quiescence to a transitional state where they reinitiate their transcriptional program and are
486 metabolically ready to be activated. Because of the highly context-dependent effect of TGF-β, the
487 final impact of galunisertib is likely heterogenous and dependent on other intrinsic and extrinsic

488 cellular stimuli. In absence of direct TCR engagement or other activation stimuli, the majority of
489 the T cells does not undergo full/classical activation and proliferation following galunisertib
490 treatment. Instead, the cells are pushed toward a more effector-like phenotype. This explains our
491 observation of an enrichment of transient effector or "transitional effector" T cells that, in turn, can
492 reinitiate viral transcription and more promptly respond to antigenic stimulation. Indeed,
493 functionally, we demonstrated that the PBMC after galunisertib treatment secrete higher levels of
494 IFN-γ and TNF-α. Interestingly, there was no increase in IL-2 secretion. The link between TGF-β
495 and IL-2(77) and the critical role of IL-2 in T cell proliferation again suggest that galunisertib
496 enhances an effector phenotype uncoupled from cellular proliferation. scRNAseq analysis
497 demonstrated a trend toward an effector phenotype also in other immune cells, such as B cells,
498 NKs and macrophages. Future studies will need to uncover in depth the effect of TGF-β blockade
499 on these other immune subsets.
500 This study has several limitations. The most important limitations are the relatively small number
501 of macaques and the lack of a concurrent untreated control group. We also could not investigate
502 in depth the viral kinetics after ART interruption because of the short follow up after ATI. An
503 additional important limitation is the lack of immunoPET/CT images from an uninfected control
504 group of macaques treated with galunisertib. This control group may have given us insight on the
505 impact of galunisertib on the pharmacokinetics of the immunoPET/CT probe in absence of
506 antigen. Moreover, we did not explore changes in the phenotype or turnover of cells isolated from
507 gut and lymph nodes and relied solely on transcriptional data for these tissues. Although we found
508 an association between TCF-1 downregulation, enhanced effector function (IFN-γ release) and
509 measures of latency reversal, a causal link between increased effector phenotype and latency
510 reversal was not definitively established. Finally, because of sample availability, we could not
511 dissect the cellular origin of increased IFN-γ and TNF-α.

512 In conclusion, we report that in vivo treatment with a clinical stage small molecule TGF-β inhibitor
513 drives a transitional effector phenotype in T cells that is likely responsible for increasing the
514 frequency of spontaneous latency reversal events, stimulating SIV-specific immune responses,
515 and decreasing the viral reservoir. Future work will determine whether the galunisertib-driven
516 enhanced antiviral responses and decreased viral reservoirs can significantly contribute to post-
517 ART virological control.
518

519 **MATERIALS AND METHODS**

520 **Study design and Ethics Statement**

521 A total of 8 adult female Indian origin *Rhesus* macaques (*Macaca mulatta*; Mamu A*01, B*08 and
522 B*17 negative) were used for the study described in the manuscript (Table S1). All the macaques
523 were selected form the colonies bred and raised at the New Iberia Research Center (NIRC),
524 University of Louisiana at Lafayette. All animal experiments were conducted following guidelines
525 established by the Animal Welfare Act and the NIH for housing and care of laboratory animals
526 and performed in accordance with institutional regulations after review and approval by the
527 Institutional Animal Care and Usage Committees (IACUC) of the University of Louisiana at
528 Lafayette (2021-8821-002; protocol 8821-01).
529 Rhesus macaques (n=8 main study + 4 separate non-concomitant study) were infected with 300
530 $TCID_{50}$ of the barcoded SIVmac239M2 stock intravenously and ART (Tenofovir [PMPA] at
531 20mg/ml, Emtricitabine [FTC] at 40mg/ml and Dolutegravir [DTG] at 2.5mg/ml) was initiated on
532 week 6 pi. Galunisertib treatment was initiated on week 35 p.i. Powder (MedChemExpress –
533 MCE, NJ, USA) was dissolved in water and given orally in a treat twice daily at 20mg/kg. 4 cycles
534 of 2 weeks daily treatment with 2 weeks wash out period were performed. Macaques 08M156
535 and A6X003 were given the rhesus recombinant antibody (rhesus/human chimeric) anti-PD1
536 antibody [NIVOR4LALA; comprising silenced rhesus IgG4k constant regions and variable regions

537 from anti-human PD-1, nivolumab; non-human primates reagents resource, NHPRR; 5mg/kg] at
538 the beginning of the 3rd and 4th galunisertib cycle.
539 Blood viral load was monitored biweekly before and during ART and every 3-4 days during
540 Galunisertib treatment. Colorectal biopsies and LN FNA were collected before and after
541 galunisertib treatment. ART was terminated 3 weeks after the last galunisertib dose and
542 euthanasia and necropsy to harvest tissues were performed at week 58 post infection, tissues
543 samples were flash frozen, fixed in OCT or Z-fix.
544
545 **Plasma and Tissue SIV Viral loads (VL)**
546 Blood was collected in EDTA tubes and plasma was separated by density gradient centrifugation
547 and used for the determination of plasma VL by SIVgag qRT-PCR at NIRC or at Leidos
548 (Quantitative Molecular Diagnostics Core, AIDS and Cancer Virus Program Frederick National
549 Laboratory). Tissue VL from snap frozen PBMC pellets, colorectal biopsies and LN FNA were
550 performed as described in (*78*). SIV-TILDA was performed on freshly stored PBMC before cycle
551 1 and at the end of cycle 4 of galunisertib by Accelevir, Baltimore, MD.
552
553 **ImmunoPET/CT**
554 ImmunoPET/CT for mapping SIV signals in total body scans were conducted in part as reported
555 previously(*44*). The probe consisted of primatized p7D3 anti-env F(ab)'2 coupled with the chelator
556 DOTA and labeled with Cu^{64} just prior to administration to the animals. For probe administration,
557 the animals were sedated, and a venous catheter was placed into an arm of leg vein to minimize
558 bleeding of the probe into the tissue surrounding the site of injection. The probe for each animal
559 consisted of ~1mg of the p7D3 F(ab)'2 labeled with 2-3 mCi of ^{64}Cu. After injection, the animals
560 were allowed to recuperate in their cage until the next day. At 24 hours, the animals were again
561 anesthetized with Telazol and the macaque's body was immobilized in dorsal recumbency on the

562 scanner table. Scans were conducted in a Phillips Gemini TF64 scanner. The final CT image was
563 compiled from 200 to 300 slices, depending on macaque size.
564 PET Image analysis was performed using the MIM software. PET/CT fusions were generated
565 scaled according to calculated Standardized Uptake Values (SUV). The SUV scale for the PET
566 scans was selected based on the overall signal intensity of the PET scans (whole body), and the
567 CT scale was selected for optimal visibility of the tissues. All images and maximum image
568 projections (MIP) were set to the same0-1.5 scale for visual comparisons. Additional details on
569 MIM analysis are described in Supplemental Methods.
570
571 **Cell isolation, flow cytometry staining, classical and high-dimensional analysis**
572 Colorectal biopsy tissues were isolated by enzymatic digestion while LN biopsies were passed
573 through a 70μm cell strainer as described in(*44*). Isolated cells were phenotyped with panels listed
574 in Supplemental Table S4. FlowJo vs 10.8 was use for both classical and high-dimesional
575 analysis. PeacoQC, FlowtSNE and FlowSOM plug-ins were used with default settings. SwiftReg
576 was used for normalization(*47*). More details on the staining procedures and analysis pipeline in
577 Supplemental Methods.
578
579 **Bulk and scRNAseq analysis**
580 For bulk RNAseq, snap frozen PBMC pellets from BC1, 1hr after first Gal dose and AC1 were
581 used for RNA extraction with the RNeasy kit with on column DNA digestion (Qiagen). Library
582 preparation was performed using TruSeq Stranded Total RNA with Ribo-Zero Globin and
583 sequencing was done with an Illumina HiSeq4000 with >20M reads/samples. Sequencing data
584 was demultiplexed and trimmed using Trimmomatic v0.36 to remove adapters and low-quality
585 reads. Trimmed reads were aligned to the Mmul10 reference genome and transcripts quantified
586 using the Hisat2-StringTie pipeline(*79*). Differential gene expression analysis using the quantified
587 gene transcripts was performed with DESeq2 R package(*80*) comparing the samples attained

588 before and after galunisertib treatment and controlling for intra-animal autocorrelation.
589 Differentially expressed genes (DEGs) were analyzed by functional enrichment analysis and gene
590 set enrichment analysis (GSEA) to identify specific pathways and molecular processes altered by
591 galunisertib.
592 The Parse pipeline and Partek software were used for scRNAseq analysis. For bulk RNAseq
593 features with <100 counts were removed, data normalized and DESeq2 was used to obtain a
594 DEG list. Genes with a false discovery rate (FDR)-adjusted p-value ≤0.05 and absolute $\log_2$ fold-
595 change (FC) (compared to BC1) above 2 were defined as significantly differentially expressed
596 (DEG). For scRNAseq analysis cells isolated from lymph nodes before (BC1) and after (AC1)
597 galunisertib were fixed with the Parse fixation kit, barcoded and sequenced at the NUseq Core.
598 The Partek software was used for scRNAseq analysis. Cells with 400-8000 features, excluding
599 features with 0 reads in >99.99 cells, were included. Scran deconvolution was used for
600 normalization and cell classification was based on gene expression. Hurdle models were used to
601 compare DEGs in each cell subset before and after galunisertib. See supplemental methods for
602 a detailed description of scRNAseq analysis and additional control analysis using Seurat R
603 package with more stringent QC cut-offs and SCTransform normalization.
604
605 **Plasma cytokines and T cell responses**
606 Cytokines in plasma (at 1:2 dilution) were measured using the NHP Cytokine 24-Plex kit by Meso
607 Scale Diagnostics (MSD) according to manufacturer instructions. Frozen PBMC collected at week
608 6 post-infection (pre-ART), right before the first galunisertib administration (BC1), at the end of
609 cycle 1 (AC1) and at the end of cycle 3 (AC3) were thawed in AIM V medium (Thermo Fisher)
610 with benzonase (Sigma) and plated on a FluoroSpot (CTL) plate pre-activated with 70% Ethanol
611 and IFN-γ, TNF-α and IL-2 capture solution. Gag, pol, and env 15-mer peptides (NIH AIDS
612 Reagents program) were prepared at two times the final concentration of 2.5μg/mL with co-
613 stimulatory reagents anti-CD28 10μg/mL and anti-CD49d 10μg/mL and added to the cells in CTL-

614 Test™ Medium. Parallel positive control of PMA (20ng/mL) and ionomycin (200ng/mL) or mock
615 DMSO solution was also plated with the stimulatory reagents. PBMCs were added at 300,000
616 cells per well. After 24hrs, the plate was washed, and incubated with detection and tertiary
617 solutions and shipped to CTL for scanning and QC.
618
619 **Statistics**
620 GraphPad Prism v10, R and Python were used for statistical analysis and data visualization.
621 Wilcoxon matched-pairs test and repeated measures ANOVA or mixed effect analysis (when the
622 data set had missing data) were used to compare the different virological and immunological
623 variables between baseline (BC1) and a single or multiple post-galunisertib time points. In Prism
624 the mixed model uses a compound symmetry covariance matrix, and is fit using Restricted
625 Maximum Likelihood (REML). Cytokine data from MSD assay were first Log transformed, then
626 normalized by subcolumn/factor in percentage with 0% as smallest value and 100% larger value
627 in each dataset. Each factor was analyzed separately with ANOVA for repeated measures and
628 Dunn's multiple comparison's post-hoc test and together by principal component analysis (PCA).
629 Holm-Sidak test was used for multiple comparison correction in all cases, but FlowSOM cluster
630 comparison where the FDR method was used. Pearson r coefficient was calculated for pairwise
631 tests of association in a correlation matrix with selected variables. For RNAseq analysis see
632 above and supplemental methods. For viral population analysis, Shannon Entropy of the viral
633 barcodes present in each sample was used to measure the diversity of the viral populations (see
634 supplemental Methods). Chi-squared tests were used in R to compare barcode composition
635 between before and after cycle time points within a tissue/macaque using paired barcode relative
636 frequencies. Unless otherwise specified p-value<0.05 was considered statistically significant.
637
638 **Data Availability Statement**

All relevant data are included in the manuscript or supplemental material. Raw data files including DICOM image files are available to be shared upon request to the corresponding author elena.martinelli@northwestern.edu. All RNA sequencing data originating from this study have been deposited in NCBI GEO under the accession code: GSE244871 For reviewers: https://www.ncbi.nlm.nih.gov/geo/query/acc.cgi?acc=GSE244871 Enter token afmricsirpmlzul into the box.

LIST OF SUPPLEMENTARY MATERIALS

Supplementary Methods

Supplementary Figure Fig. S1 to S17

Supplementary Table S1 to S6

Movies S1 to S10

650 **Acknowledgements**

651 **General:** We acknowledge the helpful staff at the New Iberia Research Center as well as the help
652 of Dr. Suchitra Swaminathan and the rest of the staff of the Flow Cytometry Core Facility at the
653 Robert H. Lurie Comprehensive Cancer Center of Northwestern University in Chicago. Moreover,
654 we thank the staff of the NUseq Core at Northwestern, and in particular Dr. Ching Man Wai and
655 Matthew Schipma for the help with RNAseq data. Finally, we thank Dr. Lifson and the Leidos staff
656 for viral load measurements as well as Dr. Laird at Accelevir for providing SIV-TILDA results in a
657 timely manner. The content of this publication does not necessarily reflect the views or policies of
658 the Department of Health and Human Services, nor does mention of trade names, commercial
659 products, or organizations imply endorsement by the U.S. Government.

660 **Funding:** This project has been funded by National Institutes of Health grant R56AI157822 to Dr.
661 Martinelli, the resource for NHP immune reagents to Dr. Villinger (R24 OD010947) for probe
662 productions and in part with federal funds from the National Cancer Institute, National Institutes
663 of Health, under Contract No. 75N91019D00024/HHSN261201500003I. The Lurie Cancer Center
664 is supported in part by an NCI Cancer Center Support Grant #P30 CA060553.

665 **Authors contributions:** EM conceptualized the studies; JK performed and analyzed flow
666 cytometry and immunePET/CT data; DB, MA, DF and SA collected and processed macaque
667 samples; MRH generated vRNA/DNA and Elispot data; RC and MV analyzed Treg/Tfh; YT and
668 TJH contributed to immunePET/CT analysis; EG, YG and EM analyzed RNAseq data; CMF, BK
669 and RLR analyzed barcode data; JA, CC, FV and EM interpreted the data and wrote the
670 manuscript.

671 **Competing interests:** The authors declare no competing interests.

672 **Data and material availability:** All data needed to evaluate the conclusions in the paper are
673 included in the manuscript and/or the supplemental material. Transcriptional profiling data (raw
674 RNAseq data) will be uploaded to GEO.

675

676 **REFERENCES**

677 1. P. Gantner, S. Buranapraditkun, A. Pagliuzza, C. Dufour, M. Pardons, J. L. Mitchell, E. Kroon,
678 C. Sacdalan, N. Tulmethakaan, S. Pinyakorn, M. L. Robb, N. Phanuphak, J. Ananworanich,
679 D. Hsu, S. Vasan, L. Trautmann, R. Fromentin, N. Chomont, HIV rapidly targets a diverse
680 pool of CD4(+) T cells to establish productive and latent infections. *Immunity* **56**, 653-668
681 e655 (2023).
682 2. J. B. Whitney, A. L. Hill, S. Sanisetty, P. Penaloza-MacMaster, J. Liu, M. Shetty, L. Parenteau,
683 C. Cabral, J. Shields, S. Blackmore, J. Y. Smith, A. L. Brinkman, L. E. Peter, S. I. Mathew, K.
684 M. Smith, E. N. Borducchi, D. I. Rosenbloom, M. G. Lewis, J. Hattersley, B. Li, J.
685 Hesselgesser, R. Geleziunas, M. L. Robb, J. H. Kim, N. L. Michael, D. H. Barouch, Rapid
686 seeding of the viral reservoir prior to SIV viraemia in rhesus monkeys. *Nature* **512**, 74-77
687 (2014).
688 3. D. Persaud, Y. Zhou, J. M. Siliciano, R. F. Siliciano, Latency in human immunodeficiency
689 virus type 1 infection: no easy answers. *J Virol* **77**, 1659-1665 (2003).
690 4. D. M. Margolis, N. M. Archin, Proviral Latency, Persistent Human Immunodeficiency Virus
691 Infection, and the Development of Latency Reversing Agents. *The Journal of infectious*
692 *diseases* **215**, S111-S118 (2017).
693 5. T. A. Wagner, S. McLaughlin, K. Garg, C. Y. Cheung, B. B. Larsen, S. Styrchak, H. C. Huang,
694 P. T. Edlefsen, J. I. Mullins, L. M. Frenkel, HIV latency. Proliferation of cells with HIV
695 integrated into cancer genes contributes to persistent infection. *Science* **345**, 570-573
696 (2014).
697 6. F. Maldarelli, X. Wu, L. Su, F. R. Simonetti, W. Shao, S. Hill, J. Spindler, A. L. Ferris, J. W.
698 Mellors, M. F. Kearney, J. M. Coffin, S. H. Hughes, HIV latency. Specific HIV integration sites
699 are linked to clonal expansion and persistence of infected cells. *Science* **345**, 179-183
700 (2014).
701 7. L. B. Cohn, I. T. Silva, T. Y. Oliveira, R. A. Rosales, E. H. Parrish, G. H. Learn, B. H. Hahn, J. L.
702 Czartoski, M. J. McElrath, C. Lehmann, F. Klein, M. Caskey, B. D. Walker, J. D. Siliciano, R. F.
703 Siliciano, M. Jankovic, M. C. Nussenzweig, HIV-1 integration landscape during latent and
704 active infection. *Cell* **160**, 420-432 (2015).
705 8. K. B. Einkauf, M. R. Osborn, C. Gao, W. Sun, X. Sun, X. Lian, E. M. Parsons, G. T. Gladkov, K.
706 W. Seiger, J. E. Blackmer, C. Jiang, S. A. Yukl, E. S. Rosenberg, X. G. Yu, M. Lichterfeld,
707 Parallel analysis of transcription, integration, and sequence of single HIV-1 proviruses. *Cell*
708 **185**, 266-282 e215 (2022).
709 9. X. Lian, K. W. Seiger, E. M. Parsons, C. Gao, W. Sun, G. T. Gladkov, I. C. Roseto, K. B. Einkauf,
710 M. R. Osborn, J. M. Chevalier, C. Jiang, J. Blackmer, M. Carrington, E. S. Rosenberg, M. M.
711 Lederman, D. K. McMahon, R. J. Bosch, J. M. Jacobson, R. T. Gandhi, M. J. Peluso, T. W.
712 Chun, S. G. Deeks, X. G. Yu, M. Lichterfeld, Progressive transformation of the HIV-1
713 reservoir cell profile over two decades of antiviral therapy. *Cell Host Microbe* **31**, 83-96
714 e85 (2023).
715 10. V. Singh, A. Dashti, M. Mavigner, A. Chahroudi, Latency Reversal 2.0: Giving the Immune
716 System a Seat at the Table. *Curr HIV/AIDS Rep* **18**, 117-127 (2021).
717 11. E. Abner, A. Jordan, HIV "shock and kill" therapy: In need of revision. *Antiviral Res* **166**, 19-
718 34 (2019).

719 12. A. Ait-Ammar, A. Kula, G. Darcis, R. Verdikt, S. De Wit, V. Gautier, P. W. G. Mallon, A.
720 Marcello, O. Rohr, C. Van Lint, Current Status of Latency Reversing Agents Facing the
721 Heterogeneity of HIV-1 Cellular and Tissue Reservoirs. *Frontiers in microbiology* **10**, 3060
722 (2019).
723 13. S. A. Yukl, P. Kaiser, P. Kim, S. Telwatte, S. K. Joshi, M. Vu, H. Lampiris, J. K. Wong, HIV latency
724 in isolated patient CD4(+) T cells may be due to blocks in HIV transcriptional elongation,
725 completion, and splicing. *Sci Transl Med* **10**, (2018).
726 14. J. D. Siliciano, R. F. Siliciano, Low Inducibility of Latent Human Immunodeficiency Virus
727 Type 1 Proviruses as a Major Barrier to Cure. *J Infect Dis* **223**, 13-21 (2021).
728 15. Y. C. Ho, L. Shan, N. N. Hosmane, J. Wang, S. B. Laskey, D. I. Rosenbloom, J. Lai, J. N.
729 Blankson, J. D. Siliciano, R. F. Siliciano, Replication-competent noninduced proviruses in
730 the latent reservoir increase barrier to HIV-1 cure. *Cell* **155**, 540-551 (2013).
731 16. E. N. Borducchi, C. Cabral, K. E. Stephenson, J. Liu, P. Abbink, D. Ng'ang'a, J. P. Nkolola, A.
732 L. Brinkman, L. Peter, B. C. Lee, J. Jimenez, D. Jetton, J. Mondesir, S. Mojta, A.
733 Chandrashekar, K. Molloy, G. Alter, J. M. Gerold, A. L. Hill, M. G. Lewis, M. G. Pau, H.
734 Schuitemaker, J. Hesselgesser, R. Geleziunas, J. H. Kim, M. L. Robb, N. L. Michael, D. H.
735 Barouch, Ad26/MVA therapeutic vaccination with TLR7 stimulation in SIV-infected rhesus
736 monkeys. *Nature* **540**, 284-287 (2016).
737 17. C. C. Nixon, M. Mavigner, G. C. Sampey, A. D. Brooks, R. A. Spagnuolo, D. M. Irlbeck, C.
738 Mattingly, P. T. Ho, N. Schoof, C. G. Cammon, G. K. Tharp, M. Kanke, Z. Wang, R. A. Cleary,
739 A. A. Upadhyay, C. De, S. R. Wills, S. D. Falcinelli, C. Galardi, H. Walum, N. J. Schramm, J.
740 Deutsch, J. D. Lifson, C. M. Fennessey, B. F. Keele, S. Jean, S. Maguire, B. Liao, E. P. Browne,
741 R. G. Ferris, J. H. Brehm, D. Favre, T. H. Vanderford, S. E. Bosinger, C. D. Jones, J. P. Routy,
742 N. M. Archin, D. M. Margolis, A. Wahl, R. M. Dunham, G. Silvestri, A. Chahroudi, J. V. Garcia,
743 Systemic HIV and SIV latency reversal via non-canonical NF-kappaB signalling in vivo.
744 *Nature* **578**, 160-165 (2020).
745 18. D. O'Sullivan, The metabolic spectrum of memory T cells. *Immunol Cell Biol* **97**, 636-646
746 (2019).
747 19. J. M. Crater, D. F. Nixon, R. L. Furler O'Brien, HIV-1 replication and latency are balanced by
748 mTOR-driven cell metabolism. *Front Cell Infect Microbiol* **12**, 1068436 (2022).
749 20. E. Besnard, S. Hakre, M. Kampmann, H. W. Lim, N. N. Hosmane, A. Martin, M. C. Bassik, E.
750 Verschueren, E. Battivelli, J. Chan, J. P. Svensson, A. Gramatica, R. J. Conrad, M. Ott, W. C.
751 Greene, N. J. Krogan, R. F. Siliciano, J. S. Weissman, E. Verdin, The mTOR Complex Controls
752 HIV Latency. *Cell Host Microbe* **20**, 785-797 (2016).
753 21. H. J. Barbian, M. S. Seaton, S. D. Narasipura, J. Wallace, R. Rajan, B. E. Sha, L. Al-Harthi,
754 beta-catenin regulates HIV latency and modulates HIV reactivation. *PLoS Pathog* **18**,
755 e1010354 (2022).
756 22. F. Gounari, K. Khazaie, TCF-1: a maverick in T cell development and function. *Nat Immunol*
757 **23**, 671-678 (2022).
758 23. J. C. Valle-Casuso, M. Angin, S. Volant, C. Passaes, V. Monceaux, A. Mikhailova, K. Bourdic,
759 V. Avettand-Fenoel, F. Boufassa, M. Sitbon, O. Lambotte, M. I. Thoulouze, M. Muller-
760 Trutwin, N. Chomont, A. Saez-Cirion, Cellular Metabolism Is a Major Determinant of HIV-
761 1 Reservoir Seeding in CD4(+) T Cells and Offers an Opportunity to Tackle Infection. *Cell*
762 *Metab* **29**, 611-626 e615 (2019).

763 24. S. A. Oh, M. O. Li, TGF-beta: guardian of T cell function. *Journal of immunology* **191**, 3973-
764 3979 (2013).
765 25. S. S. Gabriel, C. Tsui, D. Chisanga, F. Weber, M. Llano-Leon, P. M. Gubser, L. Bartholin, F.
766 Souza-Fonseca-Guimaraes, N. D. Huntington, W. Shi, D. T. Utzschneider, A. Kallies,
767 Transforming growth factor-beta-regulated mTOR activity preserves cellular metabolism
768 to maintain long-term T cell responses in chronic infection. *Immunity* **54**, 1698-1714
769 e1695 (2021).
770 26. Y. Hu, W. H. Hudson, H. T. Kissick, C. B. Medina, A. P. Baptista, C. Ma, W. Liao, R. N. Germain,
771 S. J. Turley, N. Zhang, R. Ahmed, TGF-beta regulates the stem-like state of PD-1+ TCF-1+
772 virus-specific CD8 T cells during chronic infection. *J Exp Med* **219**, (2022).
773 27. C. Ma, N. Zhang, Transforming growth factor-beta signaling is constantly shaping memory
774 T-cell population. *Proc Natl Acad Sci U S A* **112**, 11013-11017 (2015).
775 28. S. Viel, A. Marcais, F. S. Guimaraes, R. Loftus, J. Rabilloud, M. Grau, S. Degouve, S. Djebali,
776 A. Sanlaville, E. Charrier, J. Bienvenu, J. C. Marie, C. Caux, J. Marvel, L. Town, N. D.
777 Huntington, L. Bartholin, D. Finlay, M. J. Smyth, T. Walzer, TGF-beta inhibits the activation
778 and functions of NK cells by repressing the mTOR pathway. *Sci Signal* **9**, ra19 (2016).
779 29. J. S. Delisle, M. Giroux, G. Boucher, J. R. Landry, M. P. Hardy, S. Lemieux, R. G. Jones, B. T.
780 Wilhelm, C. Perreault, The TGF-beta-Smad3 pathway inhibits CD28-dependent cell growth
781 and proliferation of CD4 T cells. *Genes Immun* **14**, 115-126 (2013).
782 30. G. M. Lewis, E. J. Wehrens, L. Labarta-Bajo, H. Streeck, E. I. Zuniga, TGF-beta receptor
783 maintains CD4 T helper cell identity during chronic viral infections. *J Clin Invest* **126**, 3799-
784 3813 (2016).
785 31. A. P. Nath, A. Braun, S. C. Ritchie, F. R. Carbone, L. K. Mackay, T. Gebhardt, M. Inouye,
786 Comparative analysis reveals a role for TGF-beta in shaping the residency-related
787 transcriptional signature in tissue-resident memory CD8+ T cells. *PLoS One* **14**, e0210495
788 (2019).
789 32. N. Zhang, M. J. Bevan, Transforming growth factor-beta signaling controls the formation
790 and maintenance of gut-resident memory T cells by regulating migration and retention.
791 *Immunity* **39**, 687-696 (2013).
792 33. T. Hirai, Y. Yang, Y. Zenke, H. Li, V. K. Chaudhri, J. S. De La Cruz Diaz, P. Y. Zhou, B. A. Nguyen,
793 L. Bartholin, C. J. Workman, D. W. Griggs, D. A. A. Vignali, H. Singh, D. Masopust, D. H.
794 Kaplan, Competition for Active TGFbeta Cytokine Allows for Selective Retention of
795 Antigen-Specific Tissue- Resident Memory T Cells in the Epidermal Niche. *Immunity* **54**,
796 84-98 e85 (2021).
797 34. C. Larson, B. Oronsky, C. A. Carter, A. Oronsky, S. J. Knox, D. Sher, T. R. Reid, TGF-beta: a
798 master immune regulator. *Expert Opin Ther Targets* **24**, 427-438 (2020).
799 35. S. Samer, Y. Thomas, M. Arainga, C. Carter, L. M. Shirreff, M. S. Arif, J. M. Avita, I. Frank, M.
800 D. McRaven, C. T. Thuruthiyil, V. B. Heybeli, M. R. Anderson, B. Owen, A. Gaisin, D. Bose,
801 L. M. Simons, J. F. Hultquist, J. Arthos, C. Cicala, I. Sereti, P. J. Santangelo, R. Lorenzo-
802 Redondo, T. J. Hope, F. J. Villinger, E. Martinelli, Blockade of TGF-beta signaling reactivates
803 HIV-1/SIV reservoirs and immune responses in vivo. *JCI Insight* **7**, (2022).
804 36. S. Bergstresser, D. A. Kulpa, TGF-beta Signaling Supports HIV Latency in a Memory CD4+ T
805 Cell Based In Vitro Model. *Methods Mol Biol* **2407**, 69-79 (2022).

806 37. S. Chinnapaiyan, R. K. Dutta, M. Nair, H. S. Chand, I. Rahman, H. J. Unwalla, TGF-beta1
807 increases viral burden and promotes HIV-1 latency in primary differentiated human
808 bronchial epithelial cells. *Scientific reports* **9**, 12552 (2019).
809 38. R. B. Holmgaard, D. A. Schaer, Y. Li, S. P. Castaneda, M. Y. Murphy, X. Xu, I. Inigo, J. Dobkin,
810 J. R. Manro, P. W. Iversen, D. Surguladze, G. E. Hall, R. D. Novosiadly, K. A. Benhadji, G. D.
811 Plowman, M. Kalos, K. E. Driscoll, Targeting the TGFbeta pathway with galunisertib, a
812 TGFbetaRI small molecule inhibitor, promotes anti-tumor immunity leading to durable,
813 complete responses, as monotherapy and in combination with checkpoint blockade. *J*
814 *Immunother Cancer* **6**, 47 (2018).
815 39. D. Melisi, D. Y. Oh, A. Hollebecque, E. Calvo, A. Varghese, E. Borazanci, T. Macarulla, V.
816 Merz, C. Zecchetto, Y. Zhao, I. Gueorguieva, M. Man, L. Gandhi, S. T. Estrem, K. A. Benhadji,
817 M. C. Lanasa, E. Avsar, S. C. Guba, R. Garcia-Carbonero, Safety and activity of the TGFbeta
818 receptor I kinase inhibitor galunisertib plus the anti-PD-L1 antibody durvalumab in
819 metastatic pancreatic cancer. *J Immunother Cancer* **9**, (2021).
820 40. A. Wick, A. Desjardins, C. Suarez, P. Forsyth, I. Gueorguieva, T. Burkholder, A. L. Cleverly, S.
821 T. Estrem, S. Wang, M. M. Lahn, S. C. Guba, D. Capper, J. Rodon, Phase 1b/2a study of
822 galunisertib, a small molecule inhibitor of transforming growth factor-beta receptor I, in
823 combination with standard temozolomide-based radiochemotherapy in patients with
824 newly diagnosed malignant glioma. *Invest New Drugs* **38**, 1570-1579 (2020).
825 41. C. J. Martin, A. Datta, C. Littlefield, A. Kalra, C. Chapron, S. Wawersik, K. B. Dagbay, C. T.
826 Brueckner, A. Nikiforov, F. T. Danehy, Jr., F. C. Streich, Jr., C. Boston, A. Simpson, J. W.
827 Jackson, S. Lin, N. Danek, R. R. Faucette, P. Raman, A. D. Capili, A. Buckler, G. J. Carven, T.
828 Schurpf, Selective inhibition of TGFbeta1 activation overcomes primary resistance to
829 checkpoint blockade therapy by altering tumor immune landscape. *Sci Transl Med* **12**,
830 (2020).
831 42. M. Terabe, F. C. Robertson, K. Clark, E. De Ravin, A. Bloom, D. J. Venzon, S. Kato, A. Mirza,
832 J. A. Berzofsky, Blockade of only TGF-beta 1 and 2 is sufficient to enhance the efficacy of
833 vaccine and PD-1 checkpoint blockade immunotherapy. *Oncoimmunology* **6**, e1308616
834 (2017).
835 43. P. J. Santangelo, K. A. Rogers, C. Zurla, E. L. Blanchard, S. Gumber, K. Strait, F. Connor-
836 Stroud, D. M. Schuster, P. K. Amancha, J. J. Hong, S. N. Byrareddy, J. A. Hoxie, B. Vidakovic,
837 A. A. Ansari, E. Hunter, F. Villinger, Whole-body immunoPET reveals active SIV dynamics in
838 viremic and antiretroviral therapy-treated macaques. *Nat Methods* **12**, 427-432 (2015).
839 44. S. Samer, Y. Thomas, M. Araínga, C. Carter, L. Shirreff, M. Arif, J. Avita, I. Frank, M. McRaven,
840 C. Thuruthiyil, V. Heybeli, M. Anderson, B. Owen, A. Gaisin, D. Bose, L. Simons, J. Hultquist,
841 J. Arthos, C. Cicala, I. Sereti, P. Santangelo, R. Lorenzo-Redondo, T. Hope, F. Villinger, E.
842 Martinelli, Blockade of TGF-β signaling reactivates HIV-1/SIV reservoirs and immune
843 responses in vivo. *bioRxiv*, 2022.2005.2013.489595 (2022).
844 45. S. J. Im, B. T. Konieczny, W. H. Hudson, D. Masopust, R. Ahmed, PD-1+ stemlike CD8 T cells
845 are resident in lymphoid tissues during persistent LCMV infection. *Proc Natl Acad Sci U S*
846 *A* **117**, 4292-4299 (2020).
847 46. S. Van Gassen, B. Callebaut, M. J. Van Helden, B. N. Lambrecht, P. Demeester, T. Dhaene,
848 Y. Saeys, FlowSOM: Using self-organizing maps for visualization and interpretation of
849 cytometry data. *Cytometry A* **87**, 636-645 (2015).

850 47. J. A. Rebhahn, S. A. Quataert, G. Sharma, T. R. Mosmann, SwiftReg cluster registration
851 automatically reduces flow cytometry data variability including batch effects. *Commun*
852 *Biol* **3**, 218 (2020).
853 48. M. J. Blackburn, M. Zhong-Min, F. Caccuri, K. McKinnon, L. Schifanella, Y. Guan, G. Gorini,
854 D. Venzon, C. Fenizia, N. Binello, S. N. Gordon, C. J. Miller, G. Franchini, M. Vaccari,
855 Regulatory and Helper Follicular T Cells and Antibody Avidity to Simian Immunodeficiency
856 Virus Glycoprotein 120. *J Immunol* **195**, 3227-3236 (2015).
857 49. S. Helmold Hait, D. A. Vargas-Inchaustegui, T. Musich, V. Mohanram, I. Tuero, D. J. Venzon,
858 J. Bear, M. Rosati, M. Vaccari, G. Franchini, B. K. Felber, G. N. Pavlakis, M. Robert-Guroff,
859 Early T Follicular Helper Cell Responses and Germinal Center Reactions Are Associated
860 with Viremia Control in Immunized Rhesus Macaques. *J Virol* **93**, (2019).
861 50. Y. Zhou, B. Zhou, L. Pache, M. Chang, A. H. Khodabakhshi, O. Tanaseichuk, C. Benner, S. K.
862 Chanda, Metascape provides a biologist-oriented resource for the analysis of systems-
863 level datasets. *Nat Commun* **10**, 1523 (2019).
864 51. Z. Qiu, T. H. Chu, B. S. Sheridan, TGF-beta: Many Paths to CD103(+) CD8 T Cell Residency.
865 *Cells* **10**, (2021).
866 52. H. S. Lim, P. Qiu, Quantifying Cell-Type-Specific Differences of Single-Cell Datasets Using
867 Uniform Manifold Approximation and Projection for Dimension Reduction and Shapley
868 Additive exPlanations. *J Comput Biol* **30**, 738-750 (2023).
869 53. X. Liao, N. Sharma, F. Kapadia, G. Zhou, Y. Lu, H. Hong, K. Paruchuri, G. H. Mahabeleshwar,
870 E. Dalmas, N. Venteclef, C. A. Flask, J. Kim, B. W. Doreian, K. Q. Lu, K. H. Kaestner, A. Hamik,
871 K. Clement, M. K. Jain, Kruppel-like factor 4 regulates macrophage polarization. *J Clin*
872 *Invest* **121**, 2736-2749 (2011).
873 54. M. A. Moso, J. L. Anderson, S. Adikari, L. R. Gray, G. Khoury, J. J. Chang, J. C. Jacobson, A.
874 M. Ellett, W. J. Cheng, S. Saleh, J. J. Zaunders, D. F. J. Purcell, P. U. Cameron, M. J. Churchill,
875 S. R. Lewin, H. K. Lu, HIV latency can be established in proliferating and nonproliferating
876 resting CD4+ T cells in vitro: implications for latency reversal. *AIDS* **33**, 199-209 (2019).
877 55. J. Neidleman, X. Luo, J. Frouard, G. Xie, F. Hsiao, T. Ma, V. Morcilla, A. Lee, S. Telwatte, R.
878 Thomas, W. Tamaki, B. Wheeler, R. Hoh, M. Somsouk, P. Vohra, J. Milush, K. S. James, N.
879 M. Archin, P. W. Hunt, S. G. Deeks, S. A. Yukl, S. Palmer, W. C. Greene, N. R. Roan,
880 Phenotypic analysis of the unstimulated in vivo HIV CD4 T cell reservoir. *Elife* **9**, (2020).
881 56. A. Chitrakar, M. Sanz, S. B. Maggirwar, N. Soriano-Sarabia, HIV Latency in Myeloid Cells:
882 Challenges for a Cure. *Pathogens* **11**, (2022).
883 57. E. L. Pearce, Metabolism in T cell activation and differentiation. *Curr Opin Immunol* **22**,
884 314-320 (2010).
885 58. A. Wiercinska-Drapalo, R. Flisiak, J. Jaroszewicz, D. Prokopowicz, Increased plasma
886 transforming growth factor-beta1 is associated with disease progression in HIV-1-infected
887 patients. *Viral Immunol* **17**, 109-113 (2004).
888 59. M. Dickinson, A. E. Kliszczak, E. Giannoulatou, D. Peppa, P. Pellegrino, I. Williams, H.
889 Drakesmith, P. Borrow, Dynamics of Transforming Growth Factor (TGF)-beta Superfamily
890 Cytokine Induction During HIV-1 Infection Are Distinct From Other Innate Cytokines. *Front*
891 *Immunol* **11**, 596841 (2020).
892 60. A. S. Liovat, M. A. Rey-Cuille, C. Lecuroux, B. Jacquelin, I. Girault, G. Petitjean, Y. Zitoun, A.
893 Venet, F. Barre-Sinoussi, P. Lebon, L. Meyer, M. Sinet, M. Muller-Trutwin, Acute plasma

894 biomarkers of T cell activation set-point levels and of disease progression in HIV-1
895 infection. *PLoS One* **7**, e46143 (2012).
896 61. R. J. Salmond, Regulation of T Cell Activation and Metabolism by Transforming Growth
897 Factor-Beta. *Biology (Basel)* **12**, (2023).
898 62. S. Regis, A. Dondero, F. Caliendo, C. Bottino, R. Castriconi, NK Cell Function Regulation by
899 TGF-beta-Induced Epigenetic Mechanisms. *Front Immunol* **11**, 311 (2020).
900 63. V. Zaiatz-Bittencourt, D. K. Finlay, C. M. Gardiner, Canonical TGF-beta Signaling Pathway
901 Represses Human NK Cell Metabolism. *J Immunol* **200**, 3934-3941 (2018).
902 64. L. Das, A. D. Levine, TGF-beta inhibits IL-2 production and promotes cell cycle arrest in
903 TCR-activated effector/memory T cells in the presence of sustained TCR signal
904 transduction. *J Immunol* **180**, 1490-1498 (2008).
905 65. W. Chen, TGF-beta Regulation of T Cells. *Annu Rev Immunol* **41**, 483-512 (2023).
906 66. T. Yamazaki, A. J. Gunderson, M. Gilchrist, M. Whiteford, M. X. Kiely, A. Hayman, D. O'Brien,
907 R. Ahmad, J. V. Manchio, N. Fox, K. McCarty, M. Phillips, E. Brosnan, G. Vaccaro, R. Li, M.
908 Simon, E. Bernstein, M. McCormick, L. Yamasaki, Y. Wu, A. Drokin, T. Carnahan, Y. To, W. L.
909 Redmond, B. Lee, J. Louie, E. Hansen, M. C. Solhjem, J. Cramer, W. J. Urba, M. J. Gough, M.
910 R. Crittenden, K. H. Young, Galunisertib plus neoadjuvant chemoradiotherapy in patients
911 with locally advanced rectal cancer: a single-arm, phase 2 trial. *Lancet Oncol* **23**, 1189-
912 1200 (2022).
913 67. J. J. Harding, R. K. Do, A. Yaqubie, A. Cleverly, Y. Zhao, I. Gueorguieva, M. Lahn, K. A.
914 Benhadji, R. K. Kelley, G. K. Abou-Alfa, Phase 1b study of galunisertib and ramucirumab in
915 patients with advanced hepatocellular carcinoma. *Cancer Med* **10**, 3059-3067 (2021).
916 68. R. K. Kelley, E. Gane, E. Assenat, J. Siebler, P. R. Galle, P. Merle, I. O. Hourmand, A. Cleverly,
917 Y. Zhao, I. Gueorguieva, M. Lahn, S. Faivre, K. A. Benhadji, G. Giannelli, A Phase 2 Study of
918 Galunisertib (TGF-beta1 Receptor Type I Inhibitor) and Sorafenib in Patients With
919 Advanced Hepatocellular Carcinoma. *Clin Transl Gastroenterol* **10**, e00056 (2019).
920 69. D. Melisi, R. Garcia-Carbonero, T. Macarulla, D. Pezet, G. Deplanque, M. Fuchs, J. Trojan,
921 H. Oettle, M. Kozloff, A. Cleverly, C. Smith, S. T. Estrem, I. Gueorguieva, M. M. F. Lahn, A.
922 Blunt, K. A. Benhadji, J. Tabernero, Galunisertib plus gemcitabine vs. gemcitabine for first-
923 line treatment of patients with unresectable pancreatic cancer. *Br J Cancer* **119**, 1208-
924 1214 (2018).
925 70. T. E. Walshe, M. Saint-Geniez, A. S. Maharaj, E. Sekiyama, A. E. Maldonado, P. A. D'Amore,
926 TGF-beta is required for vascular barrier function, endothelial survival and homeostasis of
927 the adult microvasculature. *PLoS One* **4**, e5149 (2009).
928 71. H. F. Dvorak, Vascular permeability factor/vascular endothelial growth factor: a critical
929 cytokine in tumor angiogenesis and a potential target for diagnosis and therapy. *J Clin*
930 *Oncol* **20**, 4368-4380 (2002).
931 72. P. J. Santangelo, C. Cicala, S. N. Byrareddy, K. T. Ortiz, D. Little, K. E. Lindsay, S. Gumber, J.
932 J. Hong, K. Jelicic, K. A. Rogers, C. Zurla, F. Villinger, A. A. Ansari, A. S. Fauci, J. Arthos, Early
933 treatment of SIV+ macaques with an alpha(4)beta(7) mAb alters virus distribution and
934 preserves CD4(+) T cells in later stages of infection. *Mucosal Immunol* **11**, 932-946 (2018).
935 73. E. J. Fray, F. Wu, F. R. Simonetti, C. Zitzmann, N. Sambaturu, C. Molina-Paris, A. M. Bender,
936 P. T. Liu, J. D. Ventura, R. W. Wiseman, D. H. O'Connor, R. Geleziunas, T. Leitner, R. M.
937 Ribeiro, A. S. Perelson, D. H. Barouch, J. D. Siliciano, R. F. Siliciano, Antiretroviral therapy

938 reveals triphasic decay of intact SIV genomes and persistence of ancestral variants. *Cell*
939 *Host Microbe* **31**, 356-372 e355 (2023).
940 74. G. Escobar, D. Mangani, A. C. Anderson, T cell factor 1: A master regulator of the T cell
941 response in disease. *Sci Immunol* **5**, (2020).
942 75. R. L. Rutishauser, C. D. T. Deguit, J. Hiatt, F. Blaeschke, T. L. Roth, L. Wang, K. A. Raymond,
943 C. E. Starke, J. C. Mudd, W. Chen, C. Smullin, R. Matus-Nicodemos, R. Hoh, M. Krone, F. M.
944 Hecht, C. D. Pilcher, J. N. Martin, R. A. Koup, D. C. Douek, J. M. Brenchley, R. P. Sekaly, S. K.
945 Pillai, A. Marson, S. G. Deeks, J. M. McCune, P. W. Hunt, TCF-1 regulates HIV-specific CD8+
946 T cell expansion capacity. *JCI Insight* **6**, (2021).
947 76. Y. S. Choi, J. A. Gullicksrud, S. Xing, Z. Zeng, Q. Shan, F. Li, P. E. Love, W. Peng, H. H. Xue, S.
948 Crotty, LEF-1 and TCF-1 orchestrate T(FH) differentiation by regulating differentiation
949 circuits upstream of the transcriptional repressor Bcl6. *Nat Immunol* **16**, 980-990 (2015).
950 77. S. G. Zheng, J. Wang, P. Wang, J. D. Gray, D. A. Horwitz, IL-2 is essential for TGF-beta to
951 convert naive CD4+CD25- cells to CD25+Foxp3+ regulatory T cells and for expansion of
952 these cells. *J Immunol* **178**, 2018-2027 (2007).
953 78. I. Frank, M. Cigoli, M. S. Arif, M. D. Fahlberg, S. Maldonado, G. Calenda, A. Pegu, E. S. Yang,
954 R. Rawi, G. Y. Chuang, H. Geng, C. Liu, T. Zhou, P. D. Kwong, J. Arthos, C. Cicala, B. F.
955 Grasperge, J. L. Blanchard, A. Gettie, C. M. Fennessey, B. F. Keele, M. Vaccari, T. J. Hope, A.
956 S. Fauci, J. R. Mascola, E. Martinelli, Blocking alpha4beta7 integrin delays viral rebound in
957 SHIVSF162P3-infected macaques treated with anti-HIV broadly neutralizing antibodies. *Sci*
958 *Transl Med* **13**, (2021).
959 79. M. Pertea, D. Kim, G. M. Pertea, J. T. Leek, S. L. Salzberg, Transcript-level expression
960 analysis of RNA-seq experiments with HISAT, StringTie and Ballgown. *Nat Protoc* **11**, 1650-
961 1667 (2016).
962 80. M. I. Love, W. Huber, S. Anders, Moderated estimation of fold change and dispersion for
963 RNA-seq data with DESeq2. *Genome Biol* **15**, 550 (2014).
964
965
966

967 **FIGURES**

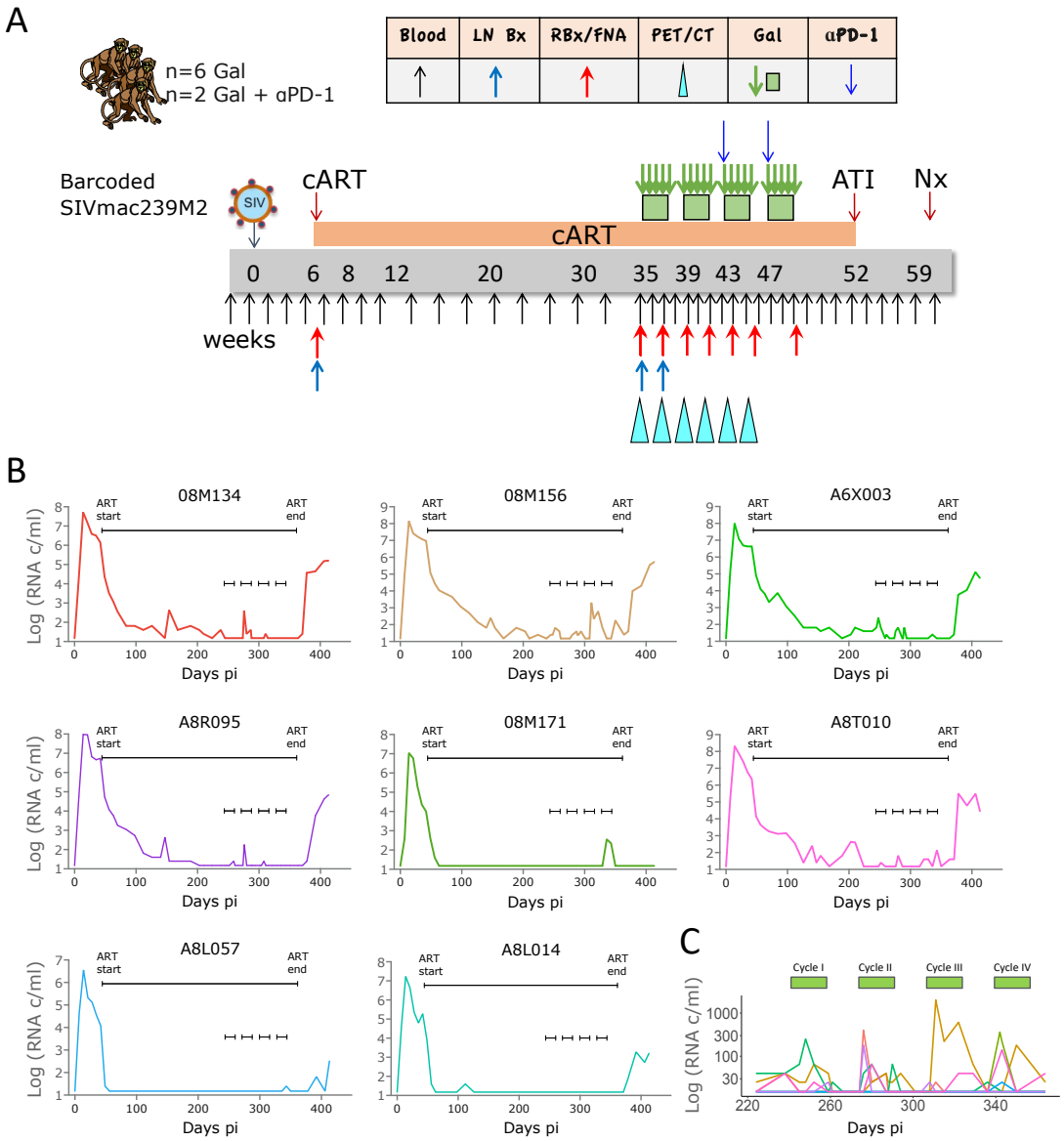

968 **Figure 1. Four 2-weeks cycles with galunisertib lead to viral reactivation in blood.** A)
969 Schematic representation of the study and sampling schedule B) Plasma VL in blood for each
970 macaque throughout the study. The longer black line indicates the period on ART, while the 4
971 small black lines indicate the start and end of each galunisertib cycle. C) Enlarged plasma VL for
972 all macaques during galunisertib therapy. Green bars indicate galunisertib cycles.

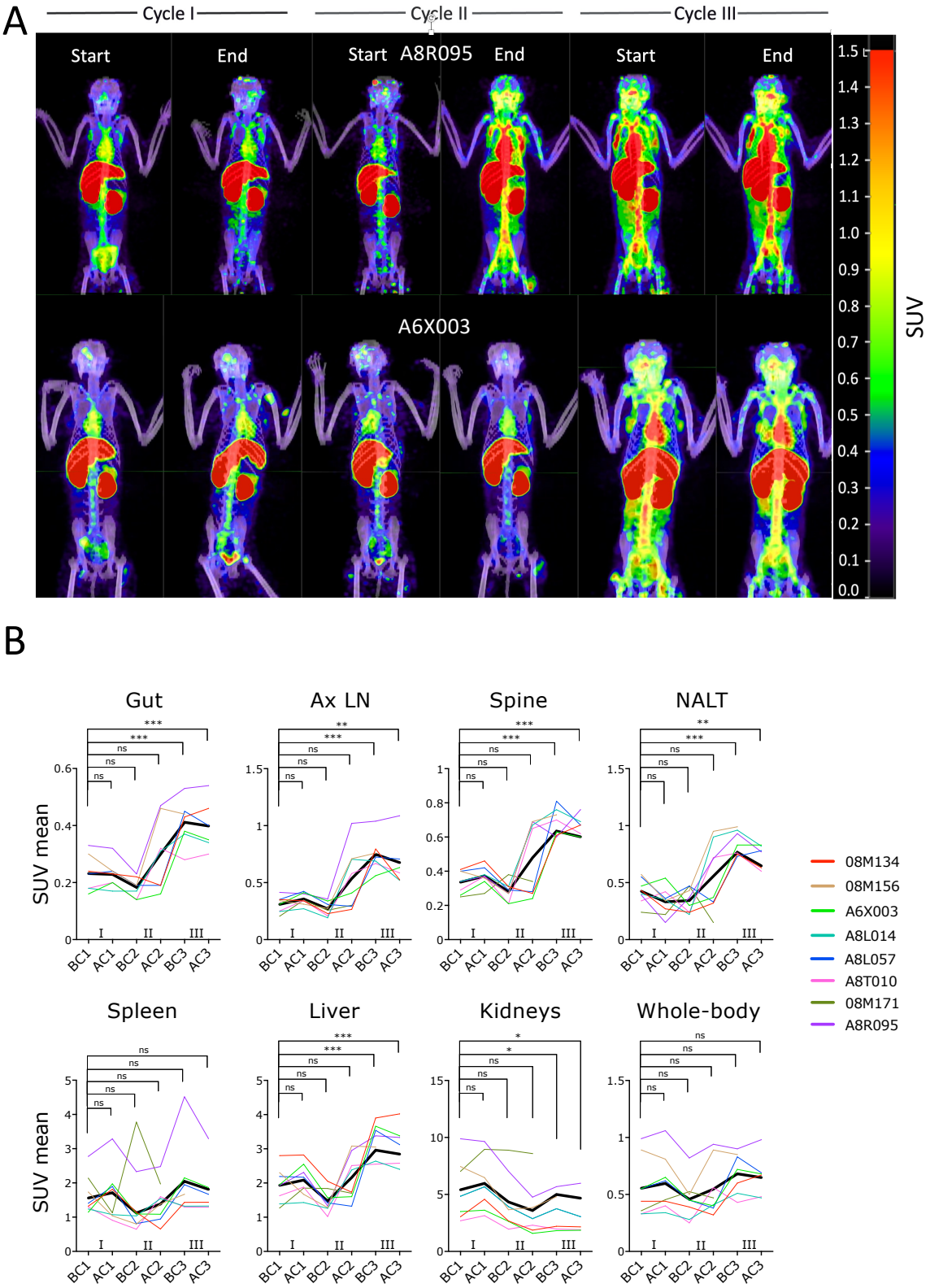

973 **Figure 2. Galunisertib leads to viral reactivation in tissues.** A) The ^{64}Cu-DOTA-Fab$_2$(7D3)

probe was injected ~24hrs before PET/CT scan before and at the end of each of the first 3 galunisertib cycles. Representative images from the maximum intensity projections (MIP) of fused PET and CT scans are show for a macaque with a major increase at the end of cycle 2 and one showing increase at the beginning of cycle 3. MIPs were generated using the MIM software, set to a numerical scale of 0-1.5 SUVbw and visualized with the *Rainbow* color scale. B) Mean SUV were calculated for each anatomical area and values analyzed with mixed-effect analysis. Data from the scans performed at the last 2 time points (BC3 and AC3) in 08M171 were excluded because of technical issues with the probe. Thicker black line represents the mean. P–values were calculated for comparison of each time point with the before cycle 1 time point (BC1; AC1= after cycle 1, BC2= before cycle 2; AC2= after cycle 2; BC3= before cycle 3; AC3= after cycle 3; Holm-Sidak multiple comparison correction; *$p \leq 0.05$ **$p \leq 0.01$ ***$p \leq 0.01$)

986

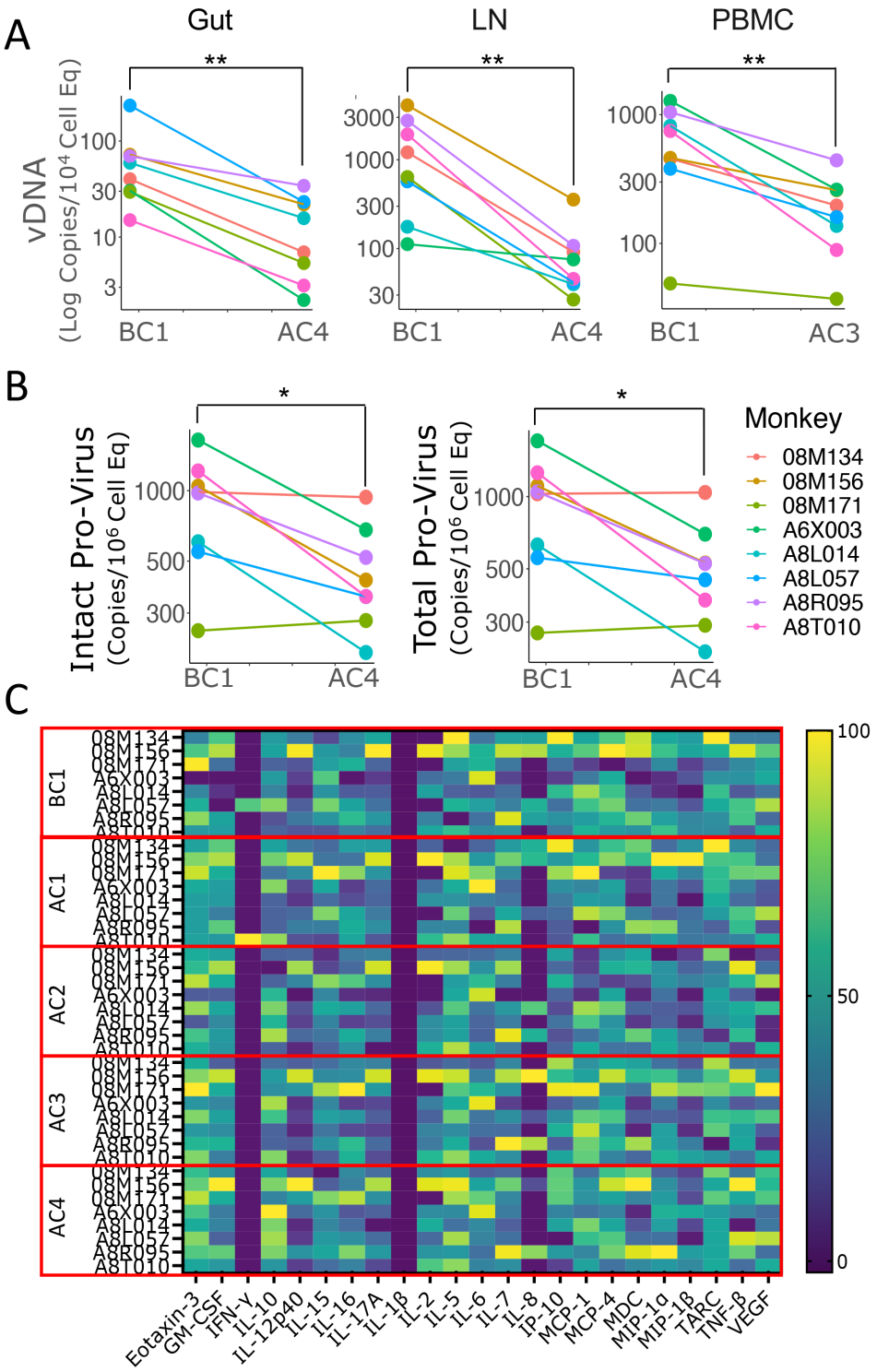

987 **Figure 3. Galunisertib decreases viral reservoir in absence of systemic inflammation.** A)

988 Levels of cell-associated (CA)-vDNA per cell equivalent are shown for the time point before cycle

989 1 (BC1) and at the end of cycle 3 (AC3) or 4 (AC4) for the respective tissues. B) IPDA data are
990 shown for intact and total provirus for BC1 and AC4 in PBMC. pvalues are shown for Wilcoxon
991 matched pair signed-rank non-parametric test (*p≤0.05 **p≤0.01 ***p≤0.01) C) Heat map of
992 cytokine concentration in plasma at the indicated time point are shown after Log transformation
993 and normalization. Statistical analysis was run on each factor separately and together (no
994 significant differences after multiple comparison adjustment).

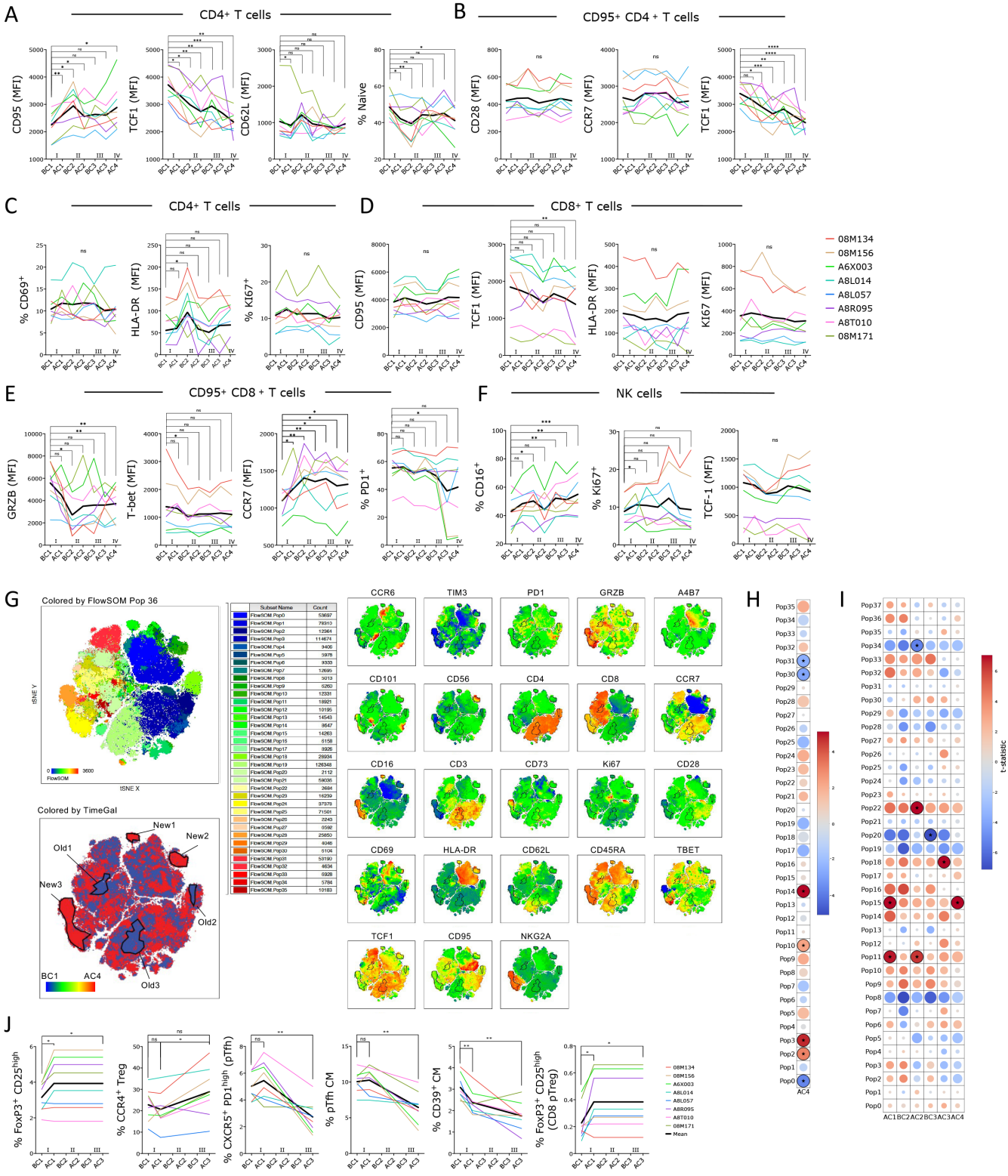

995 **Figure 4. Galunisertib leads toward effector in T and NK cells, increasing Treg and**

996 **decreasing Tfh frequencies.** A-F) Geometric mean fluorescent intensities (MFI) of each marker
997 and frequency of indicated subset within live, singlets $CD3^+$ $CD4^+$ T cells (A and C) or $CD3^+$ $CD4^+$
998 $CD95^+$ T cells (B) or $CD8^+$ or $CD8^+$ $CD95^+$ T cells or NK cells ($NKG2A^+$ $CD8^+$ $CD3^-$ cells) are
999 shown. Thick black line represents the mean. Changes from baseline (beginning of cycle 1, BC1)
1000 are shown for graphs with at least 1 significant difference (Repeated measures ANOVA with Holm-
1001 Sidak correction; *p≤0.05 **p≤0.01 ***p≤0.01). G) tSNE of lymphocyte, live, singlets events after
1002 normalization for BC1 and AC4 (all 8 macaques) with FlowSOM 36 clusters overlaid on tSNE (top
1003 left) or heatmap of each markers MFI (right) or heatmap of time point (blue is BC1 and red is AC4;
1004 bottom left) is shown. 6 populations were manually gated on red or blue areas (red, New1-3 and
1005 blue Old1-3). H) Bubble chart displaying changes in AC4 from BC1 in populations (FlowSOM
1006 clusters) characterized by markers MFI in Fig S8A. Color is proportional to the effect size and size
1007 to p-value (Wilcoxon sum rank non-parameter test). I) Bubble chart displaying changes from BC1
1008 at all time points in populations (FlowSOM clusters) characterized in Fig S8C (ANOVA repeated
1009 measures with Holm-Sidak correction; *p≤0.05 **p≤0.01 ***p≤0.01). J) Frequency of indicated
1010 subset within live, singlets $CD3^+$ $CD4^+$ T or $CD3^+$ $CD4^+$ $CD95^+$ $CD28^+$ T cells (CM=central
1011 memory) or within $CD3^+$ $CD8^+$ T cells. Changes from baseline (BC1) are shown (ANOVA repeated
1012 measures with Holm-Sidak correction for multiple comparisons; *p≤0.05 **p≤0.01 ***p≤0.01).
1013

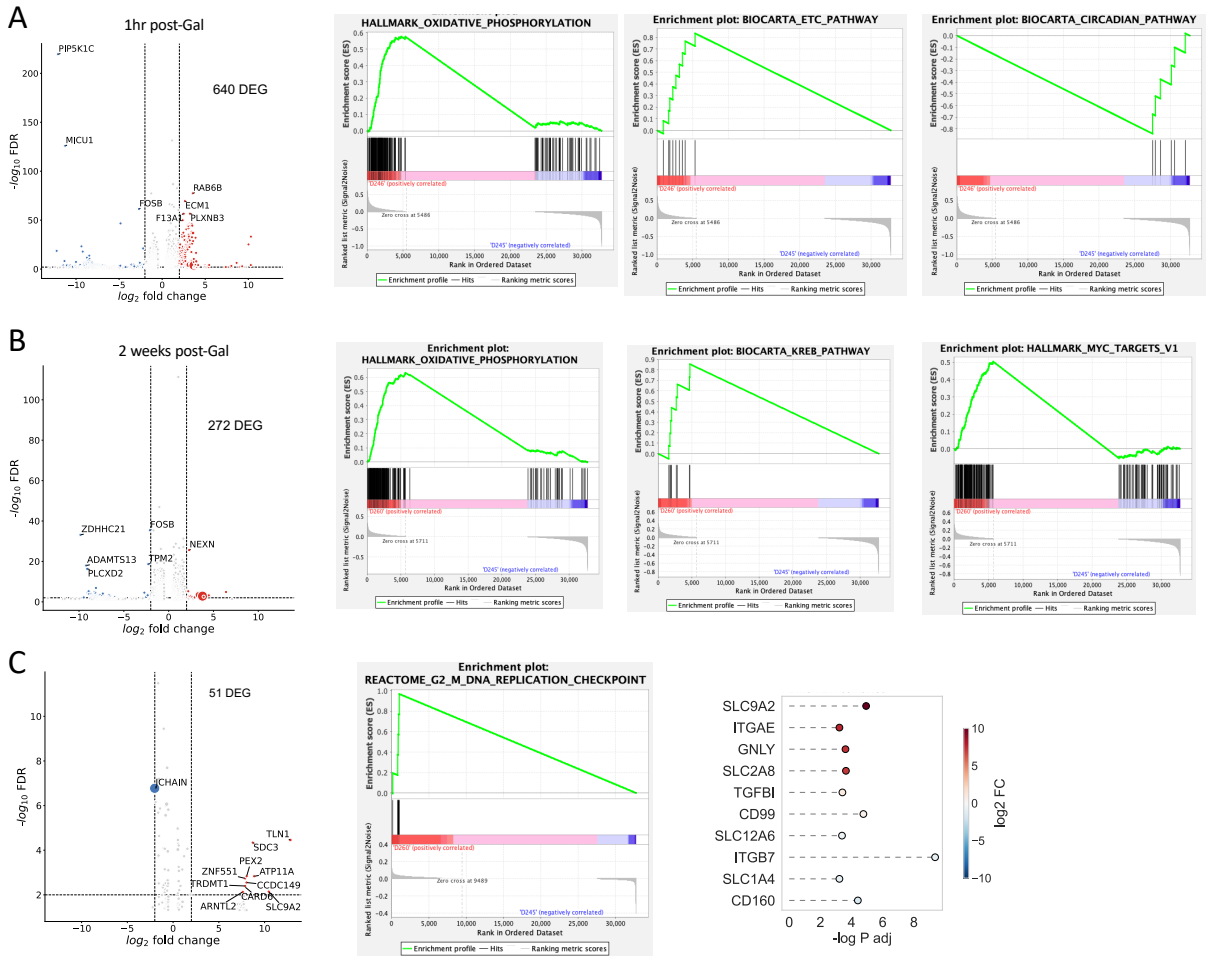

Figure 5. OXPHOS and other metabolic pathways increase rapidly with TGF-β blockade. A-C) Bulk RNAseq was performed with PBMC from before cycle 1 (24hrs) and 1hrs after the first dose of galunisertib (A) or after the last dose of cycle 1 (B) and with rectal biopsies collected before cycle 1 (24hrs) and after the last dose of cycle 1 (C). The number of differentially expressed genes (DEG) with an FDR <0.05 and abs(log_2FC)>2 are shown in each respective volcano plot. Enrichment plots are shown after GSEA (with all FDR<0.05 DEGs) for significantly enriched pathways (top 1 or 2 pathway by ES). C) Lollipop graph of selected DEG of interest among significantly different genes (FDR<0.05).

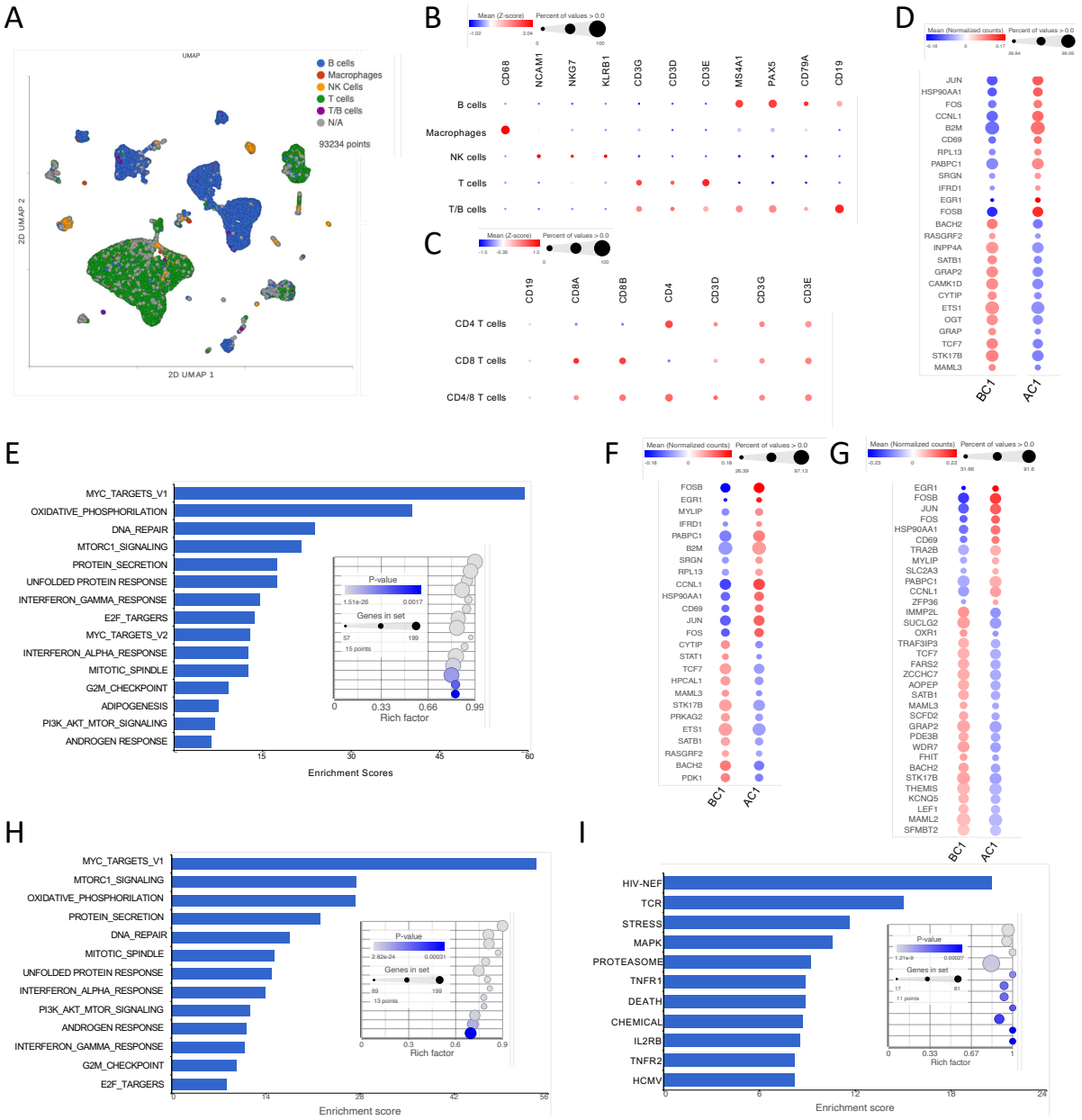

1023 **Figure 6. scRNAseq of lymph node before and after cycle 1 confirms a switch toward**
1024 **effector and increased metabolism in all immune subsets with galunisertib.** A) UMAP
1025 projection of 93234 cells from lymph nodes collected right before and at the end of cycle 1 from
1026 all 8 macaques (16 samples). Gene-based classification of major immune subset is overlaid on
1027 UMAP. In gray are unclassified cells. B-C) Bubble plots showing expression (mean normalized
1028 counts proportional to the color; size proportional to the percentage of cells) of each marker listed

1029 in each cell subset. Marker listed are those used for classification of major immune subsets (B)
1030 or CD4$^+$ and CD8$^+$ T cells (C). D) Significantly different genes (FDR<0.05; log2FC=0.15) in the T
1031 cell subset are shown with color proportional to normalized counts. E) Significantly enriched
1032 pathways (FDR<0.01) in T cells DEGs within the hallmark collection. F-G) Significantly different
1033 genes (FDR<0.05; log2FC=0.15) in the CD4$^+$ (F) and CD8$^+$ (G) T cell subset. H-I) Significantly
1034 enriched pathways (FDR<0.01) in CD4$^+$ T cells DEGs within the hallmark (H) and biocarta (I)
1035 collections.
1036

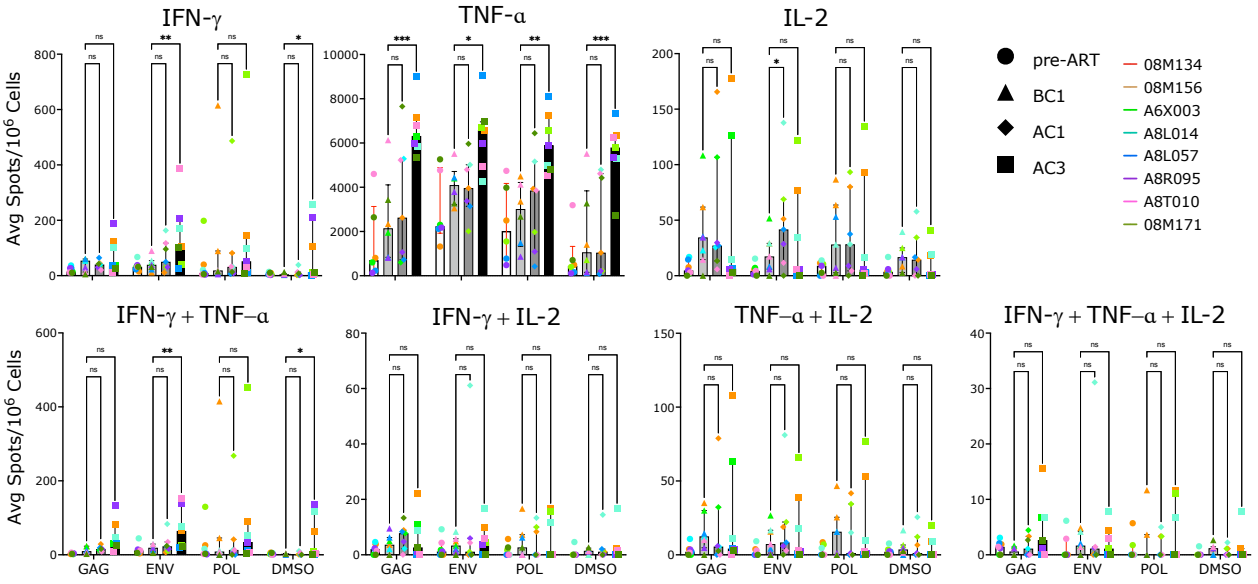

1037 **Figure 7. Galunisertib increases SIV-specific responses.** Average spots (from triplicates) per
1038 10^6 PBMC at the time of ART initiation (pre-ART), before cycle 1 (BC1), after cycle 1 (AC1) and
1039 at the end of cycle 3 (AC3) with galunisertib after 24hrs ex vivo stimulation with 15-mer peptides
1040 (gag, env, pol) or mock (DMSO). Each post-galunisertib time point was compared to BC1 (Mixed
1041 effect analysis with Dunnet post-hoc p-values are shown; *p≤0.05 **p≤0.01 ***p≤0.001)

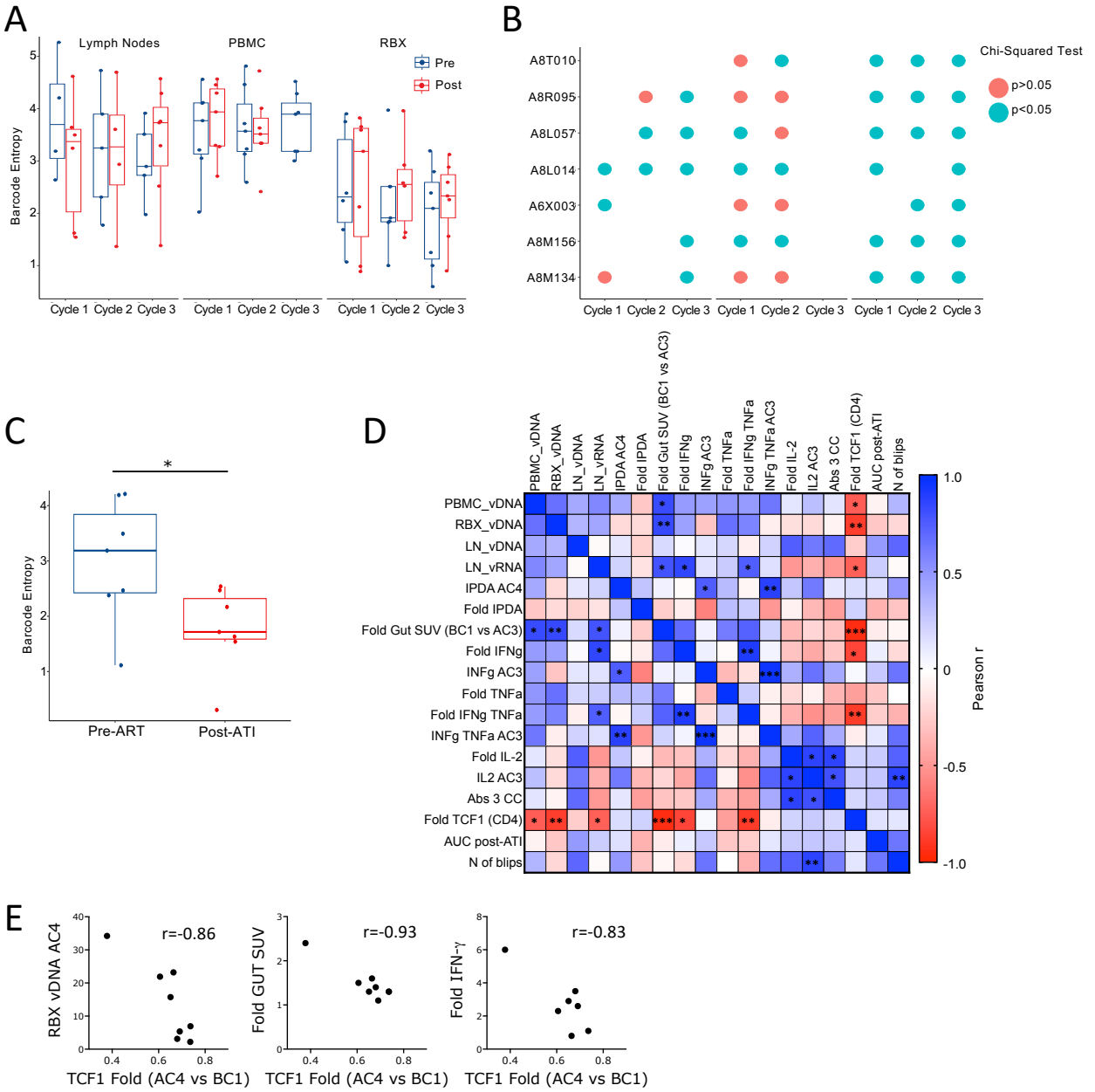

Figure 8. TCF1 decrease associates with virological and immunological endpoints. A) Barcode diversity measure as Shannon Entropy is shown before and after each of the first 3 galunisertib cycles for LN, PBMC and colorectal biopsies. Box-and-whisker plot represents the median +/− the interquartile range (no significant differences using linear mixed effects models). Blue= before; Red= end of each cycle. B) Bubble plot shows the results of statistical testing (Chi-squared) for differences in frequency distribution of barcodes before compared to after, for each

1049 of the first 3 cycles of galunisertib for each macaque in the indicated tissues. Blue indicates
1050 significant differences $p \leq 0.05$. C) Barcode entropy of virus isolated at the time of ART initiation
1051 compared to week 6 post-ATI in plasma (Wilcoxon matched pairs test; $^{*}p \leq 0.05$). D) Correlation
1052 matrix of several key variables of virological or immunological effect of galunisertib. Color is
1053 proportional to Pearson r coefficient. $^{*}p \leq 0.05$ $^{**}p \leq 0.01$ $^{***}p \leq 0.001$ indicate significant correlations.
1054 F) Association between fold increase in TCF1 (MFI) from BC1 to AC4 with CA-vDNA levels at
1055 AC4, change in gut SUV at AC3 compared to BC1 and fold increase in IFN-γ (AC3 vs BC1).
1056 Person r is shown. All correlations have $^{*}p \leq 0.05$.